remote sensing

MDPI

Article

Reconstructing Lake Storage for the Major Water Bodies in the Aral Sea Basin Using Multi-DEM Hypsometry

Shuangyan Huang [1], Xi Chen [2,3], Liao Yang [2,3], Tie Liu [2,3], Longhui Li [4], Xuexi Ma [5,6], Bing Yue [7], Nannan Wu [5], Akhylbek K. Kurishbayev [8], Imanmadi Duman [9], Hossein Azadi [5,10] and Xiaoting Ma [5,6,*]

[1] Postdoctoral Research Station, Zhejiang University of Technology, Hangzhou 310014, China; huangshuangyan15@mails.ucas.ac.cn
[2] College of Geoinformatics, Zhejiang University of Technology, Hangzhou 310014, China; chenxi@ms.xjb.ac.cn (X.C.); yangliao@zjut.edu.cn (L.Y.); liutie@ms.xjb.ac.cn (T.L.)
[3] Moganshan Geospatial Information Laboratory, Huzhou 313299, China
[4] School of Geography, Nanjing Normal University, Nanjing 210023, China; longhui.li@njnu.edu.cn
[5] Xinjiang Institute of Ecology and Geography, Chinese Academy of Sciences, Urumqi 830011, China; maxx@ms.xjb.ac.cn (X.M.); wunannan@ms.xjb.ac.cn (N.W.)
[6] Research Center for Ecology and Environment of Central Asia, Chinese Academy of Sciences, Beijing 100101, China
[7] State Key Laboratory of Tibetan Plateau Earth System, Environment and Resources (TPESER), Institute of Tibetan Plateau Research, Chinese Academy of Sciences, Beijing 100101, China; bingyue18@mails.ucas.ac.cn
[8] The National Academy of Sciences of the Republic of Kazakhstan, Almaty 050010, Kazakhstan; rector@kaznaru.edu.kz
[9] Scientific and Educational Technology Platform, Kazakh National Agrarian Research University, Almaty 050010, Kazakhstan; imanmadi.duman@kaznaru.edu.kz
[10] Department of Geography, Ghent University, 9000 Ghent, Belgium; hossein.azadi@ugent.be
* Correspondence: maxiaoting@ms.xjb.ac.cn

Highlights

What are the main findings?

- We develop a multi-DEM hypsometry framework to reconstruct near-monthly lake storage for 1993–2024, recovering storage during low-level periods without bathymetric surveys.
- Reconstructed changes agree with independent satellite altimetry (r = 0.93 for level and 0.90 for storage), outperforming above-water-only and conventional model-selection baselines.

What are the implications of the main findings?

- Under whole-lake modeling, the Copernicus-based reconstruction provides a cumulative storage change of −214.30 km^3, closest to the satellite altimetry estimate of −210.68 km^3.
- Other DEMs overestimate the 1993–2024 cumulative loss by 66.15–141.01 km^3; sub-lake modeling reduces this bias and provides an SRTM-based cumulative change of −248.38 km^3.

Check for updates

Academic Editor: Tomaž Podobnikar

Received: 25 January 2026
Revised: 27 February 2026
Accepted: 1 March 2026
Published: 3 March 2026

Abstract

In arid-zone water resource management and water-security assessment, changes in water-body volume are key indicators of water availability and regulation performance. However, arid-zone lakes often lack sufficient bathymetric information to constrain geometry under low lake-level conditions. Shrinkage-driven hydrological disconnection can destabilize extrapolation of water level–storage relationships. This increases uncertainty in quantifying long-term storage changes. Here, we develop a multi-digital elevation model (DEM) hypsometry framework to reconstruct near-monthly lake storage for 1993–2024, recovering storage during low-level periods without bathymetric surveys. Reconstructed changes agree with independent satellite altimetry (r = 0.93 for level and 0.90 for storage), outperforming above-water-only (r ≈ 0.637 for water level) and conventional model-selection base-lines (r ≈ 0.753 for water level). The framework was quantified across three scenarios: expanding lakes, lake systems and reservoirs, and terminally shrinking lakes. For the persistently shrinking Big Aral Sea, under the whole-lake modeling assumption, the Copernicus-based reconstruction provides a cumulative storage change of $-214.3\ \mathrm{km}^3$, closest to the satellite altimetry estimate of $-210.68\ \mathrm{km}^3$ among the tested DEMs. In contrast, other DEMs overestimate the 1993–2024 cumulative loss by 66.15–141.01 km^3. Sub-lake modeling further adjusts the Shuttle Radar Topography Mission (SRTM)-based cumulative change to $-248.38\ \mathrm{km}^3$, substantially reducing structural bias caused by lake disconnection. This study provides a transferable technical framework for lake storage reconstruction in arid regions under degraded low lake-level conditions and hydrological disconnection.

Keywords: Aral Sea Basin; multi-DEM hypsometry; water storage reconstruction; hydrological disconnection; low lake-level conditions

---

1. Introduction

Water storage changes in arid-zone lakes and reservoirs directly affect water security, ecosystem stability, and irrigation operations. Long-term monitoring is a foundation for regional water-resource management and water-security assessment. Precipitation is scarce, and evapotranspiration is strong in these regions. As a result, these water bodies are more sensitive to climate change and human disturbance [1]. Over recent decades, arid-region lakes have experienced frequent seasonal desiccation [2]. In some regions, seasonal variability is even comparable to interannual variability [3]. The Aral Sea Basin is a representative region for arid-zone lake change in Central Asia. Climate change and human activities have driven the Aral Sea's extreme shrinkage [4] and reshaped the regional water-resource pattern at the basin scale [5]. Consequently, area-only monitoring cannot resolve two key issues: (i) the magnitude of interannual water-storage change, and (ii) whether storage can be tracked continuously during historical low-water periods when ecological risks are highest.

Quantitative estimates of lake level and water storage often rely on bathymetric surveys or stage–storage curves. The high cost of field measurements makes these data difficult to obtain in data-scarce regions [6]. This motivates remote-sensing approaches that do not require in situ bathymetry [7]. Recent studies mainly fall into three frameworks. The first framework derives bathymetry from geometric or geophysical attributes. For example, the GLOBathy dataset provides static lake-basin priors for more than 1.4 million water bodies worldwide [8]. However, for very large or complex lake basins, storage estimates are highly sensitive to terrain detail and statistical assumptions, and the uncertainty still requires explicit quantification [9]. The second framework combines water area with multi-source altimetry elevation measurements to estimate volume change [10]. This approach can provide accurate long-term water levels, but its spatial coverage is constrained by altimetry ground tracks and revisit times. The third framework uses digital elevation models (DEMs) to characterize lake-basin topography and to build empirical relationships among area, elevation, and storage change. It does not rely on bathymetric data; therefore, it has been widely applied at regional scales [11]. However, it is sensitive to the acquisition timing of the selected DEM, and remains uncertain under extreme shrinkage or hydrological disconnection.

In DEM-based long-term storage reconstruction, accuracy depends on whether DEMs provide sufficient geometric constraints under low lake-level conditions. Uncertainties in water level and storage estimates are often highest under low-stage conditions. When the lake surface retreats into the water mask at the time of DEM acquisition, the nearshore topography that controls low-stage geometry becomes unobserved. This reduces available geometric information and weakens the stability of the reconstructed time series [12]. Without an effective strategy, terminal lakes may show observation gaps during extreme shrinkage, making accuracy difficult to guarantee [13]. To address this, some studies leverage periods when the lakebed is fully exposed during DEM acquisition. They combine exposed lakebed elevations with dynamic land–water boundaries to infer water depth and water-surface elevation. They then validate the results externally with ICESat and ICESat-2 altimetry [14]. Other studies infer lake-basin topography by integrating multi-source DEM constraints [15,16] with historical multi-temporal lake boundaries [17]. This extends the geometric relationships into the low lake-level range. However, under extreme shrinkage and lake disconnection, comparability and consistency are still rarely assessed systematically.

Against this background, low-water stages often lack reliable terrain constraints, and lake disconnection can destabilize stage–storage extrapolation. These issues hinder robust long-term storage reconstruction. We therefore use five major water bodies in the Aral Sea Basin as the study area and focus on three hypotheses. H1 (multi-DEM consensus): whether multi-source DEM consensus screening with physics-consistency filters significantly reduces cross-DEM extrapolation instability. H2 (sub-lake topology): whether sub-lake modeling systematically reduces structural storage bias caused by lake disconnection and missing low-elevation detail in early DEMs. H3 (transferability): whether the framework, using only open EO-data, yields comparable reconstructions across expanding, regulated, and terminally shrinking water bodies. To test these, we reconstruct near-monthly water storage time series for 1993–2024 across all five water bodies and evaluate each hypothesis with quantitative evidence.

2. Materials and Methods

2.1. Study Area

The Aral Sea Basin (ASB) in Central Asia has a typical continental climate. Its landscape combines high mountains in the east with lowlands and deserts in the west, creating a clear topography–climate gradient (Figure 1). The western lowlands are hotter and drier, with little precipitation. The eastern mountains are cold and dry but relatively wet [18]. The Karakum and Kyzylkum Deserts are the driest parts of the basin and show the strongest evapotranspiration. Two transboundary rivers, the Amu Darya and Syr Darya, form the main hydrologic corridors that sustain the evolution of the water bodies across the basin. Lakes and reservoirs are unevenly distributed. We examine five major water bodies that represent typical hydro-geomorphic settings, including terminal lakes, expanding lakes, lake systems and reservoirs: Big Aral Sea (BAS), Small Aral Sea (SAS), Sarygamysh Lake (SARY), Aydar–Arnasay Lake System (AALS), and Chardarya Reservoir (CHR). CHR and AALS lie on the Tianshan foreland at higher elevations, about 200–300 m. Whereas BAS, SAS, and SARY sit in low-elevation terminal depressions, mostly below 50 m a.s.l. Under an arid climate, such elevation differences can amplify contrasts in how these water bodies respond to water-balance perturbations. To capture changes in lake-basin morphology and hydrologic connectivity, especially the stage-wise disconnection during the Aral Sea retreat, we define Lake Modeling Units (LMUs; Figure 1e) for geometric modeling. The LMUs include SAS, SARY, CHR, and AALS as independent units. For BAS, we further separate the western and eastern basins (WBAS and EBAS) to reflect geometric heterogeneity after lake disconnection. For BAS and SAS, boundaries are approximated by shoreline vectors from the 1960s. This allows the LMUs to include historical lakebed areas exposed during shrinkage, making better use of terrain information across stages and thereby reducing uncertainty under low lake-level conditions.

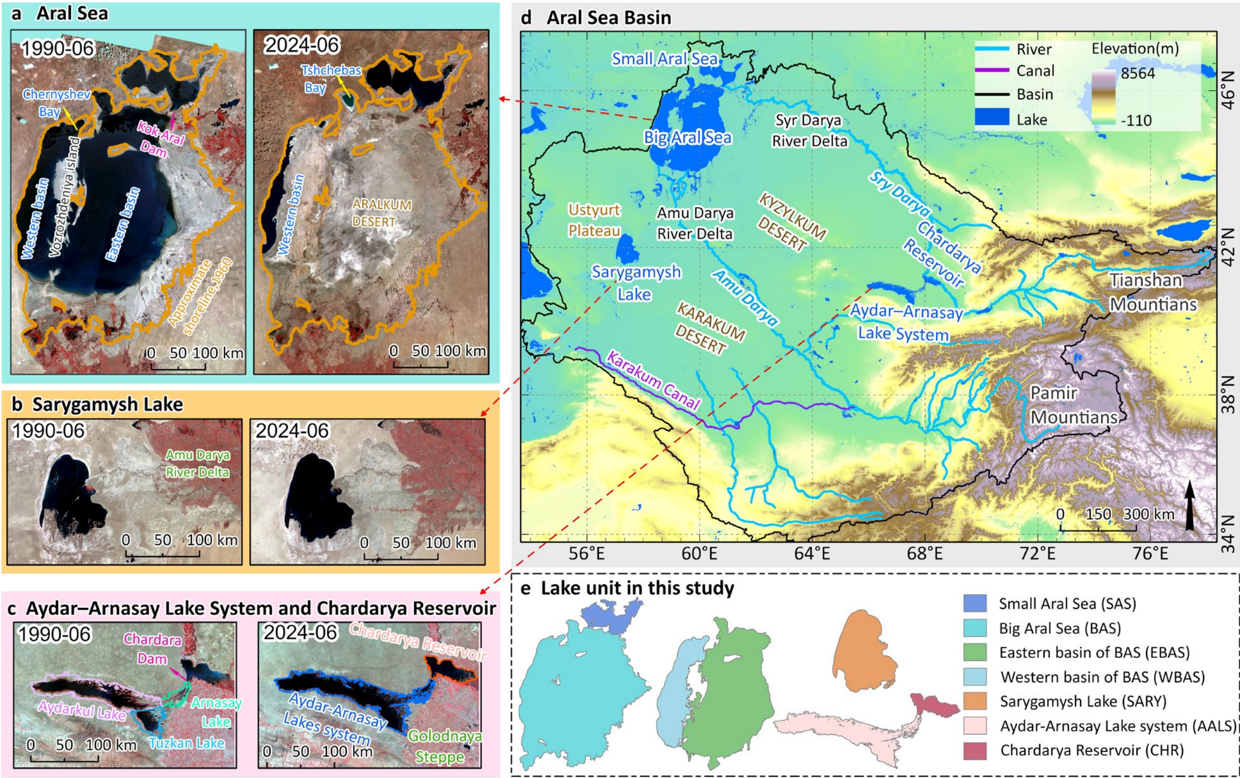

Figure 1. Study area and Lake Modeling Unit (LMU) definition in the Aral Sea Basin. (**a**–**c**) False-color Landsat composites from June 1990 and June 2024 showing morphological changes in (**a**) the Aral Sea, (**b**) Sarygamysh Lake, and (**c**) the Aydar–Arnasay Lake System and Chardarya Reservoir. (**d**) Basin topography and the locations of the study sites, the black arrow indicates true north. (**e**) Schematic of the LMUs, defining the spatial domains used for volume modeling.

2.2. Data Sources and Processing

2.2.1. Digital Elevation Models

We use five publicly available global DEM products to represent lake-basin topography and surrounding terrain in the Aral Sea Basin. These datasets span acquisition epochs from 2000 to 2015. They include two acquisition techniques: radar interferometry (InSAR) and optical stereophotogrammetry. Specifically, we use SRTM (Shuttle Radar Topography Mission) [19] and its reprocessed product NASADEM (NASA Digital Elevation Model) [20], as well as ASTER GDEM (ASTER Global Digital Elevation Model) [21], ALOS AW3D30 (ALOS World 3D 30 m) [22], and Copernicus (Copernicus Digital Elevation Model) DEM [23]. These products differ in their original design goals, processing chains, and error characteristics. Detailed parameters [24] and the corresponding Google Earth Engine (GEE) asset IDs are provided in Table 1. To ensure comparability across data sources under a common spatial reference, we reproject all DEMs to UTM Zone 41N and resample to a 30 m grid. We harmonize vertical datums by shifting EGM96-referenced DEMs to EGM2008 using the NGA geoid model. This ensures that hypsometry extraction and subsequent H–A–V construction use a unified vertical datum. Vertical accuracy ranges from ~4 m (Copernicus) to ~17 m (ASTER; Table 1), reflecting differences in sensor type and processing chain that directly affect hypsometric curve reliability at low lake-level stages.

2.2.2. Optical Imagery

Lake surface-area observations were derived from the Landsat optical archive [25] (1993–2024), including Landsat 5 TM, Landsat 7 ETM+, Landsat 8 OLI, and Landsat 9 OLI-2. In the arid environments of the Aral Sea Basin, water mapping is challenged by two common sources of interference. First, salt crusts, exposed lakebeds, and shallow water often co-occur, causing spectral confusion along shorelines. Second, cloud, snow and ice cover in winter and early spring reduce water–land separability and limit the availability of usable scenes. Sensor-specific issues and varying imaging conditions further lead to uneven temporal sampling. For example, the Landsat 7 Scan Line Corrector (SLC) failure introduces data gaps during part of the record and locally reduces the fraction of valid pixels. As a result, monthly observations are generally sparse, with missing months and pronounced seasonal-to-decadal differences in data availability. We therefore constructed a near-monthly lake surface-area time series for subsequent inference of lake-level and storage changes. Missing months were retained as gaps without interpolation to preserve the observational record. Procedures for water classification and quality control are described in Section 2.3.4.

Table 1. Specifications and Google Earth Engine (GEE) asset IDs for the multi-source DEM datasets used in this study.

Dataset	Acquisition Method	Acquisition Period	GEE Asset ID	Original Vertical Datum	Spatial Resolution	Vertical Precision
SRTM	C-band InSAR	2000	USGS/SRTMGL1_003	EGM96	1 arc-second	~9 m
NASADEM	C-band InSAR	2000	NASA/NASADEM_HGT/001	EGM96	1 arc-second	~9 m
ASTER	Optical Stereo	2000–2013	projects/sat-io/open-datasets/ASTER/GDEM	EGM96	1 arc-second	~17 m
ALOS	Optical Stereo	2006–2011	JAXA/ALOS/AW3D30/V4_1	EGM96	1 arc-second	~5 m
Copernicus	X-band InSAR	2010– 2015	COPERNICUS/DEM/GLO30	EGM2008	1 arc-second	<4 m

2.2.3. G-REALM Satellite Altimetry Observations

To independently validate the reconstructed lake levels and storage changes, we used the Global Reservoir and Lake Monitor (G-REALM) satellite altimetry dataset distributed via the USDA-FAS IPAD platform. G-REALM is mainly based on the TOPEX/Poseidon and Jason-series radar altimetry missions. It provides water-surface elevation time series at an approximately 10-day repeat cycle and is widely used for long-term lake-level assessment [26]. In this study, we used the original 10-day observations, removed outliers, and aggregated the data to monthly values. Missing months were retained as gaps without interpolation to preserve the observational record.

In the Big Aral Sea region, G-REALM provides two virtual stations (Figure 2). The East Aral station has the longest continuous record (1992–present), covering the period before complete separation in 2009, when the eastern and western basins were effectively hydraulically connected. Hence, this station was used to represent the Big Aral Sea as a whole (BAS) in this study. During the 2005–2009 transition period, observations indicate that water levels on both sides remained largely synchronous. The east station was therefore used to validate both the BAS whole-lake model and the EBAS sub-lake model, maximizing the value of the available observations. To validate the evolution of the East Basin (EBAS), we set the validation period for this station to 2005–present. The west station was used exclusively to validate the West Basin (WBAS), with the validation period starting in 2005 to capture the full transition from gradual separation to subsequent independent evolution. Additionally, we compared G-REALM water levels with the CAWATER historical water-level series (http://www.cawaterinfo.net/aral/data/index.htm, accessed on 28 February 2026) to confirm the separation chronology used above (Figure 2).

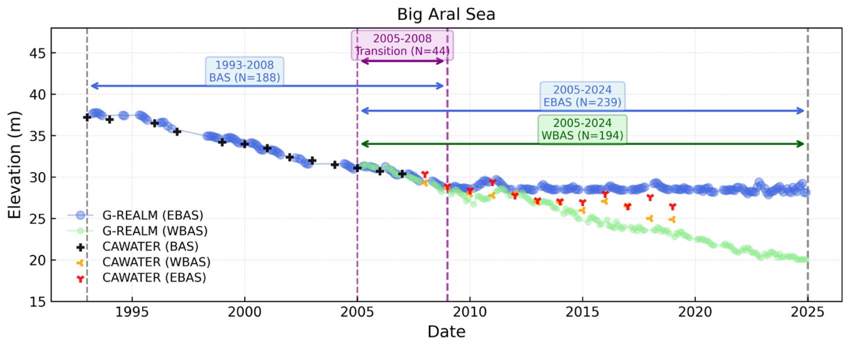

Figure 2. G-REALM water-level records for BAS, EBAS, and WBAS, with the CAWATER historical water-level series for consistency checking. N denotes the number of monthly G-REALM observations used in this study.

2.3. Methods

We propose a framework to reconstruct long-term water-level and storage changes by integrating multi-source DEM constraints with Landsat-derived area time series. As shown in Figure 3, the framework includes five modules. We first define Lake Model Units to represent fragmentation and evolving connectivity. We then derive a near-monthly area time series for 1993–2024 from Landsat imagery. Next, we reconstruct bathymetry by extracting above-water terrain from multi-source DEMs and inferring submerged geometry to fill low-water gaps. These constraints are integrated through joint model construction to link water level, area, and storage. Finally, we apply a two-stage model-selection strategy and validate the results against G-REALM satellite altimetry to produce the reconstructed time series. Detailed procedures are described in the following subsections.

2.3.1. Quantifying Geometric Differences Among Multi-Source DEMs

To quantify the consistency of different DEMs over key geomorphic segments of the lake basin, we compare elevation profiles along representative transects for each lake. Because DEM errors are terrain-dependent, a single basin-wide statistic may miss differences in geometrically critical segments [27]. We therefore define a slope-controlled segment, S_{slope}, along the median profile, where slope variability is most pronounced. This segment corresponds to the top 10% of transect positions with the largest absolute slope, and represents the portion where lake-basin geometry is most sensitive to the water level–area relationship. Within S_{slope}, we compute the cross-DEM elevation range at each transect position, and use its 95th percentile as a summary metric of multi-source DEM geometric differences, defined as follows:

$$\Delta E_{slope,95} = P_{95}\left(\max_{d} z_d(x) - \min_{d} z_d(x)\right),\ x \in S_{slope}, \tag{1}$$

Here, $z_d(x)$ denotes the elevation from the DEM indexed by d at profile position x, and P_{95} is the 95th percentile of the cross-DEM elevation range across S_{slope}. The percentile metric reduces sensitivity to local extremes and improves cross-site comparability [28].

2.3.2. Constructing Above-Water Hypsometric Constraints

To address the lack of terrain information at low water levels, we adopt an "above-water modeling–below-water inference–joint fitting" framework. First, we construct discrete above-water constraint samples (S, H, ΔV). As shown in Figure 4, the DEM provides layered topographic information above the water surface, allowing area, elevation, and storage to be mapped under a common geometric reference [9]. A key prerequisite is to determine the water-surface elevation at the time of DEM acquisition, H_0. To this end, we use a robust mode-estimation approach. We analyze the elevation frequency distribution within the lake mask, bin elevations into 1 m intervals, and take the modal elevation as H_0. This procedure reduces the influence of noise and outliers. Based on H_0, we set a vertical step of ΔH = 1 m and compute the cumulative water-surface area S_i for each elevation layer. The volume increment between adjacent layers, ΔV, is approximated using the frustum approximation:

$$\Delta V = \frac{1}{3}(H_{i+1} - H_i) \times \left(S_i + S_{i+1} + \sqrt{S_i \times S_{i+1}}\right), \tag{2}$$

where S_i and S_{i+1} are the cumulative areas at elevations H_i and H_{i+1}, respectively. In this way, we obtain a set of discrete samples for each DEM, which serves as the data basis for fitting a continuous hypsometry function.

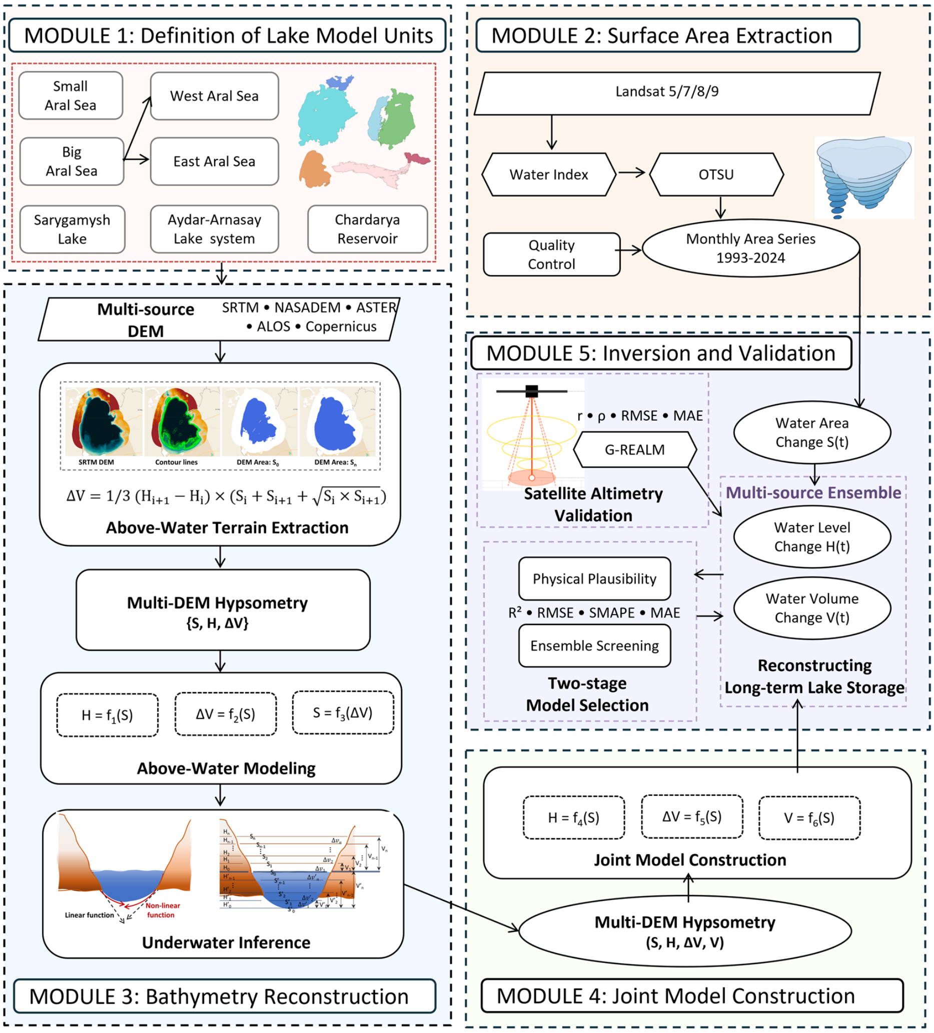

Figure 3. Workflow and module structure of the proposed framework.

2.3.3. Below-Water Inference and Joint Model Construction

Based on the discrete constraint samples extracted above, we first fit three baseline empirical relationships: H = f1(S), ΔV = f2(S), S = f3(ΔV). Each relationship is fitted independently using 1st–3rd order polynomials via ordinary least squares (OLSs). We then apply k-fold cross-validation and select the best-performing model by standard metrics (R^2, RMSE, SMAPE, MAE) to exclude obviously overfitted candidates. To enable below-water inference, we define a basin-floor boundary. Specifically, we define the basin-floor area S'_0 as the area at which $\Delta V = 0$ under $S = g(\Delta V)$, and determine the corresponding basin-floor elevation H'_0 (Figure 4b). We then use the above-water discrete samples to construct H = h(S) and extend the level–area relationship from the basin floor to the water surface. This inferred below-water segment is merged with the original DEM samples in the above-water domain, yielding a physically consistent dataset (S, H, ΔV, V). To reduce dependence on a single functional form, we refit candidate models on the merged dataset using multiple function families, including 1st–3rd order polynomials, piecewise linear interpolation (PWL), and piecewise cubic Hermite interpolation (PCHIP). We then construct three final relationships, H = f4(S), V = f5(S), and ΔV = f6(S), so that both the above-water observation domain and the below-water inference domain are represented within a unified geometric-constraint framework. To ensure physically plausible extrapolation toward low water levels, candidate functions are strictly constrained to be smooth and monotonic. To reduce potential elevation-datum inconsistencies among data sources, we define storage change as a relative increment referenced to the first valid observation month in 1993 (t_0). We focus on relative trends rather than absolute magnitudes. Finally, given the near-monthly water-surface area series S(t), we map it to lake level H(t) and storage change V(t) using the fitted models H = h(S) and V = f(S), and then compute ΔV(t).

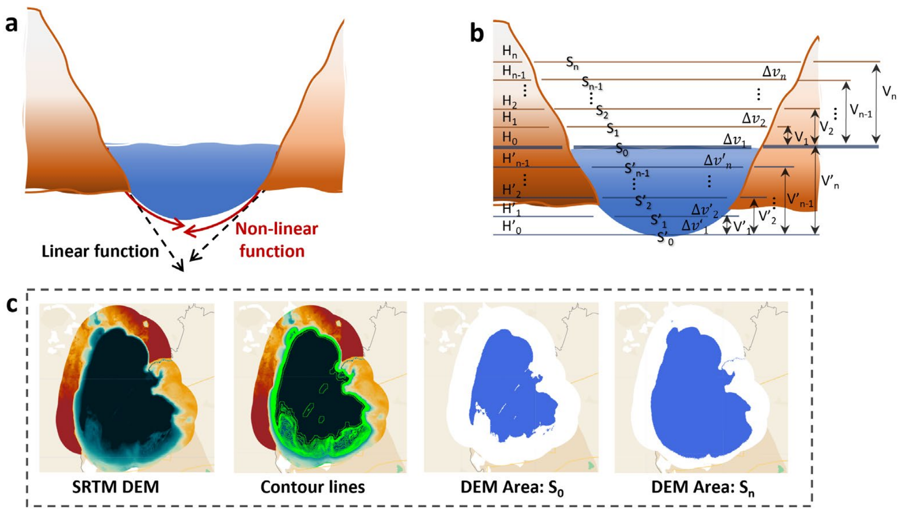

Figure 4. Schematic of bathymetry inference and hypsometry-based storage estimation. (**a**) Conceptual comparison of linear and non-linear functions for low-stage bathymetry extrapolation. (**b**) Volume accumulation scheme based on the frustum formula for above-water observed layers and below-water inferred layers. (**c**) Extraction of hypsometric curves (area–elevation-volume) from DEM slices.

2.3.4. Near-Monthly Surface Water Area Time Series

The near-monthly surface-water area time series was derived from the Landsat archive (TM, ETM+, OLI/OLI-2) for 1993–2024. We first mask clouds and cloud shadows using QA bands, and then generate a monthly representative image by median compositing all available observations within each calendar month. To reduce local voids caused by limited winter–spring coverage and Landsat 7 SLC-off gaps, we apply a temporal-buffer filling strategy that supplements missing pixels with nearby observations within a ±10-day window around the target month. We compute NDWI and related water-enhancement indices on the monthly image and extract water masks using adaptive thresholding. Thresholds are determined using the Otsu method on index histograms [29], with an NDVI constraint to suppress false positives from vegetation and wet salt crusts. For large water bodies and adjacent shallow flats, high background reflectance can distort histograms and bias scene-wide thresholds. We therefore estimate thresholds within a buffer zone around each water body and apply additional index criteria in a few unstable subregions to restore deep-water connectivity. Monthly water masks are aggregated to the

Lake Modeling Unit (LMU) scale to derive the surface-water area time series. We perform anomaly detection and manual screening; months affected by residual clouds, snow/ice, or nonphysical shapes are flagged and retained as gaps without interpolation. To support seasonal interpretation, we also compute water-occurrence frequency and delineate stable water extents. These products are used only to illustrate seasonal rhythms and spatial patterns and are not used as quantitative inputs to S(t).

2.3.5. Two-Stage Model Selection and Sub-Lake Modeling

To ensure robust reconstruction under data-scarce conditions, we adopt a two-stage strategy combining physics-consistency constraints with ensemble-consensus ranking, fully leveraging terrain information from multi-source DEMs without relying on external altimetry during model selection. For each lake, 625 candidate models are generated by combining five DEMs with multiple hypsometric function families, and monthly water level, area, and storage time series are inverted accordingly.

Stage 1 applies three physics-consistency hard filters: (i) the minimum pairwise Spearman rank correlation among area, water level, and storage must exceed 0.95; (ii) the fraction of months in which area and water level move in opposite directions must not exceed 0.02; and (iii) non-positive storage values are not permitted. Of the 625 candidates, 403 pass Stage 1 (pass rate 64.5%).

Stage 2 operates independently within each lake–DEM group. A quality filter retains candidates satisfying R^2(H–A) ≥ 0.4, RMSE(H–A) ≤ 2 m and $\leq 10\%$ of the group water-level range, MAE ≤ 5 m, and SMAPE $\leq 50\%$, reducing the pool to 354 of the 403 Stage 1 survivors (87.8%). Each retained candidate is then ranked by a joint score J, computed as

$$J = \alpha\, R_{\text{temporal}} + (1-\alpha) R_{fit}, \quad \alpha = 0.9, \tag{3}$$

$$R_{temporal} = \sum\nolimits_{k=1}^{5} w_k z_k, \tag{4}$$

$$R_{fit} = {}^{1}\!/_{2} \left[\text{prank}_{\text{g(RMSE(H–A))}} + \text{prank}_{\text{g(RMSE(V–A))}} \right], \tag{5}$$

where $z_k = \frac{|x_k - med(\{x_k\})|}{MAD(\{x_k\}) + \varepsilon}$, x_k is the k-th endpoint, and $med(\{x_k\})$ and $MAD(\{x_k\})$ are the within-group median and median absolute deviation. $prank_{g(\cdot)}$ is the within-group empirical percentile rank (0 best, 1 worst). The endpoint weights w are 0.18, 0.32, 0.14, 0.14, 0.23 for H_{start}, V_{start}, H_{end}, V_{end}, ΔV_{rel}, respectively. The candidate with the lowest J is selected as the representative model, and the Top-5 are retained as a backup pool. A cross-DEM consistency check is then applied to net storage change: if any group's ΔV deviates from the cross-DEM median by more than the median's own absolute value, the representative is replaced by the closest Top-5 alternative. This check flags 2 out of 35 groups; the remaining 33 pass without modification.

In particular, to address hydrological disconnection driven by Aral Sea shrinkage and to capture heterogeneous evolution across sub-lake basins, we implement two parallel schemes: whole-lake modeling under a single-topology assumption, and sub-lake modeling under a multi-topology assumption. In sub-lake modeling, we construct and invert the geometric relationships for the WBAS and EBAS basins independently, and then obtain total storage by volume summation $V_{\text{total}} = V_{\text{EBAS}} + V_{\text{WBAS}}$. This design keeps the geometric assumptions stage-consistent with the evolving hydrologic connectivity of the fragmented lake.

2.3.6. Inversion Validation and Uncertainty Assessment

To validate the accuracy of the reconstructed water level and storage, we use G-REALM satellite altimetry observations as an independent reference. Because timing mismatches between DEM acquisition and altimetry observations are common, direct comparisons of absolute elevations and storage may not reflect true temporal changes. We therefore reference both series to the first overlapping valid month by subtracting their values in that month. This shifts validation from absolute magnitudes to relative changes in water level and storage over time. Altimetry-referenced storage changes are computed by combining G-REALM water levels with the Landsat-derived area series and by applying the frustum formula. Finally, using the aligned and renormalized series, we quantify inversion accuracy with a set of complementary metrics. We use the Pearson correlation coefficient (r) and the Spearman rank correlation coefficient (ρ) to assess temporal synchrony and linear association between reconstructed and observed series. We use the root mean square error (RMSE) and mean absolute error (MAE) to quantify differences in magnitude. Together, these metrics provide the basis for evaluating performance across DEM sources and inversion models. In addition, we quantified uncertainty in the Landsat-derived area input. Otsu-derived areas were evaluated against manually delineated reference extents for four sub-lakes across multiple epochs (1993–2020), and agreement was quantified using R^2, median absolute percentage error (MdAPE), MAE, and mean signed bias. Area uncertainty from a $\pm$0.5-pixel shoreline assumption [30] was propagated through the fitted H–A and V–A relationships and verified with a 1000-perturbation Monte Carlo test.

2.3.7. Time-Series Trend Analysis and Change-Point Detection

To quantify the long-term evolution of hydrologic variables, we apply nonparametric methods to analyze trends and detect change points in the time series of area, water level, and storage change. For each water body, we apply the sequential Mann–Kendall test to each DEM-based inversion result to identify change points. This approach determines the change point from the intersection of the forward sequence (UF(k)) and the backward sequence (UB(k)), and uses $|UF(k)| > 1.96$ as the significance threshold. We estimate trend magnitude using Sen's slope on annual mean values to mitigate seasonal fluctuations. This estimator is robust to outliers and computes the median of slopes between all data pairs. We then conduct trend analysis separately for periods before and after the detected change point, and compare hydrologic evolution across different stages.

3. Results

3.1. Consistency and Differences in Lake-Basin Constraints Across Multi-Source DEMs

Figure 5a–c shows consistent geomorphic patterns across the five DEMs. However, they differ markedly in internal lake-basin texture and in the nearshore transition zone. Copernicus preserves the clearest microtopographic layering within the BAS lake basin. SRTM and NASADEM appear smoother over the same area. In SARY, ALOS exhibits diagonal stripe artifacts and mosaicking seams, with poorer elevation consistency within the water body. ASTER GDEM shows high-frequency noise in multiple areas. The profiles in Figure 5d further indicate that the DEMs closely agree over the flat basin-floor segment. Disagreements concentrate on both the shore slopes and the slope-break transition zone. SRTM and NASADEM show synchronous and smooth profile shapes. Copernicus shows sharper slope breaks. ASTER shows short-wavelength serrations near slope breaks, which markedly increase profile roughness. ALOS shows local depressions and spikes in areas such as CHR. These features increase local elevation spread among DEM profiles. The slope-controlled metric $\Delta E_{slope,95}$ in Table 2 corroborates these differences. ASTER shows the largest dispersion across profiles (4.94–10.45 m) and is the main source of ensemble divergence. ALOS uncertainty amplifies with terrain complexity. It is 2.52–2.84 m in the BAS, but rises to 6.44 m in the steeper CHR. By contrast, SRTM, NASADEM, and Copernicus mostly cluster approximately 2–3 m. Overall, multi-source DEM differences do not mainly reflect shifts in the macroscopic framework. They mainly reflect slope-segment detail that controls the sensitive end of the *H*–*A* relationship.

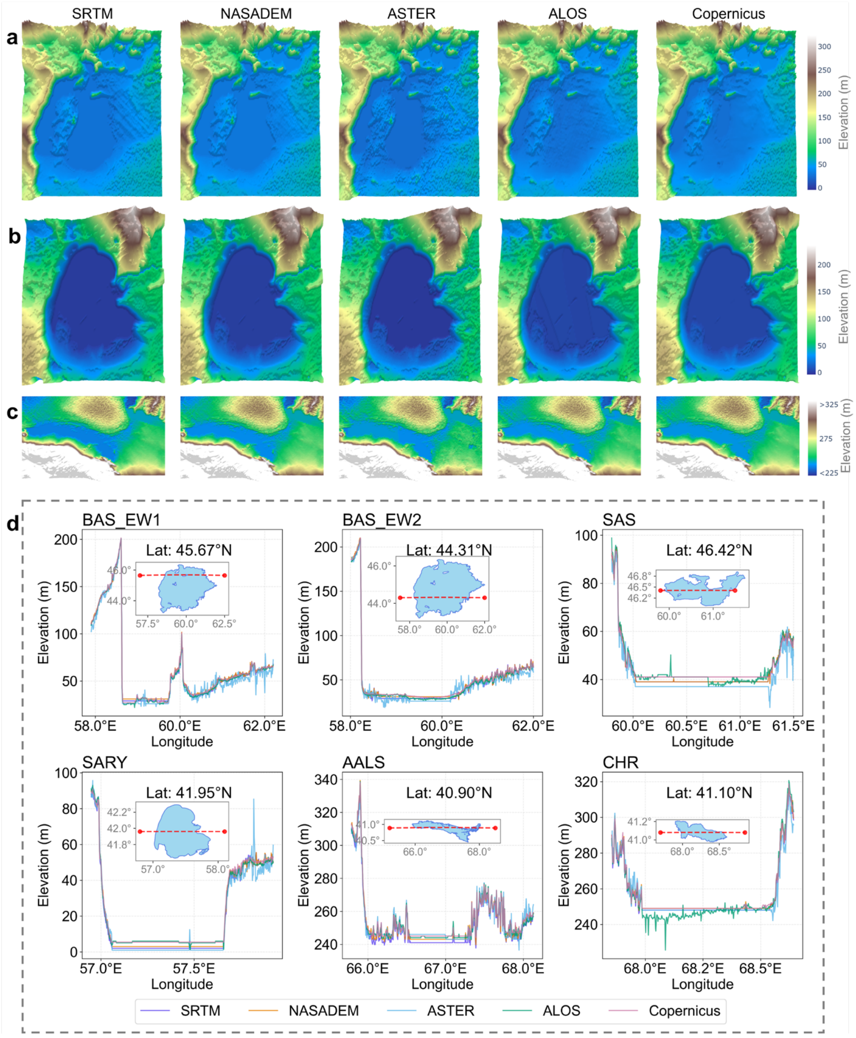

Figure 5. Three-dimensional terrain views and representative elevation profiles from five DEMs for the study of water bodies. (**a**–**c**) Three-dimensional views of basin topography and surrounding terrain derived from SRTM, NASADEM, ASTER, ALOS, and Copernicus; color scales indicate elevation (m). (**d**) Elevation profiles extracted along representative transects for each water body, highlighting cross-DEM differences in basin shape and slope structure. Transect locations are shown in the inset maps.

Table 2. Multi-DEM slope-related geometric differences along elevation profiles of the water bodies.

DEM Profile	SRTM	NASADEM	ASTER	ALOS	Copernicus
BAS_EW1	2.83	2.31	4.94	2.84	2.68
BAS_EW2	3.14	3.37	5.55	2.52	2.44
SAS	2.10	2.49	7.37	2.70	2.91
SARY	4.61	3.10	5.19	4.22	2.43
AALS	2.92	2.89	6.58	2.14	2.54
CHR	2.94	2.54	10.45	6.44	2.92

Note: Values are $\Delta E_{slope,95}$(m), the 95th percentile of the cross-DEM elevation range along each profile, representing DEM-dependent uncertainty in lake-basin geometry.

3.2. Independent Validation and Ablation Analysis Against G-REALM Altimetry

Figure 6 presents cross-water-body validation of the area series and the reconstructed water level and storage against G-REALM altimetry. It also includes ablation experiments to isolate the contribution of key components. As an input-side check, the near-monthly area series shows very high agreement with G-REALM water-surface elevation (Figure 6a;

r = 0.962, ρ = 0.951). This indicates that the area series captures both the phase and relative amplitude of water-level change. In contrast, the GSWE Monthly History shows weaker correspondence with altimetry water level (Figure 6d; r = 0.480, ρ = 0.581). This further supports our area product as a more reliable area input. For output validation, the reconstructed water-level change ΔH closely matches the altimetry-derived ΔH (Figure 6b; r = 0.93, ρ = 0.923). Storage change ΔV computed from the V–A relationship also agrees well with ΔV inferred from altimetry (Figure 6c; r = 0.90, ρ = 0.899). Together, these results validate the effectiveness of our near-monthly water level–storage reconstruction framework. The ablation analysis highlights the necessity of below-water geometric extrapolation and multi-source DEM constraints. When modeling uses only the above-water DEM range, agreement in reconstructed ΔH drops markedly (Figure 6e; r = 0.637, ρ = 0.608). This indicates that missing below-water constraints distort low-water extrapolation. Further, even with below-water reconstruction, selecting a single model using conventional statistics (highest R^2, lowest RMSE) still underperforms our framework (Figure 6f; r = 0.753, ρ = 0.748). These results suggest that R^2/RMSE-based selection alone cannot ensure stable extrapolation. Multi-source DEM and multi-model consensus constraints reduce overfitting and improve long-term consistency and transferability.

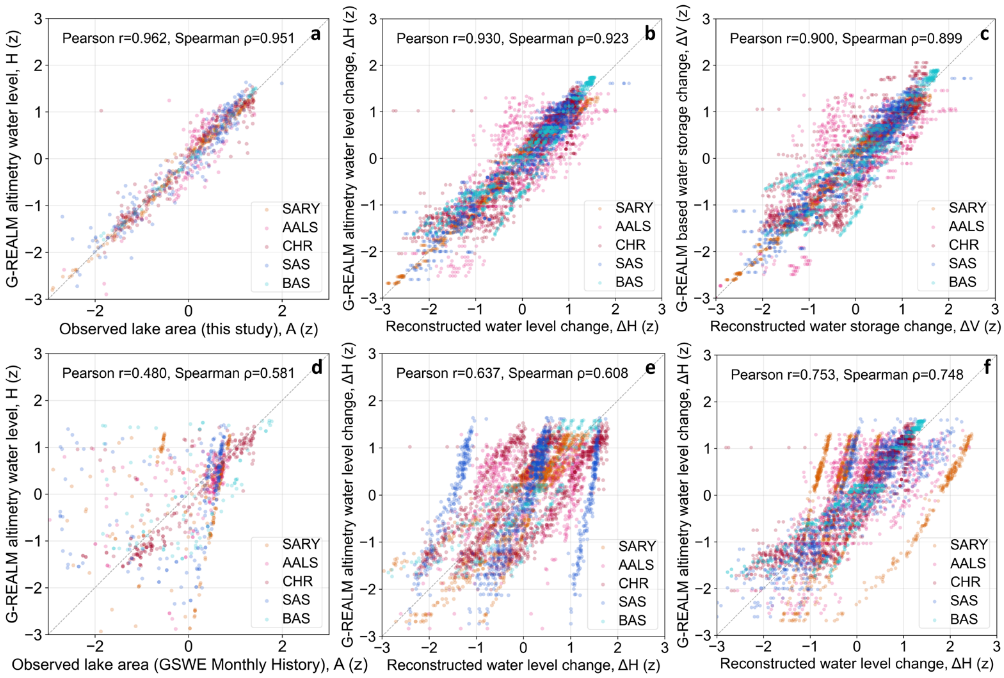

Figure 6. Independent validation of the reconstructions against G-REALM altimetry, together with two ablation baselines. (**a**) Comparison between G-REALM water-surface elevation (H) and lake area (A) derived in this study. (**b**) Comparison between altimetry-derived water-level change (ΔH) and reconstructed ΔH from the proposed framework. (**c**) Comparison between altimetry-derived storage change (ΔV) and reconstructed ΔV. (**d**) Same as (**a**), but replacing our area series with GSWE Monthly History area series. (**e**) Above-water-only baseline that reconstructs ΔH using relationships constrained by the above-water DEM range. (**f**) Conventional model-selection baseline after below-water reconstruction, where the model is selected using highest R^2 and lowest RMSE. All variables are z-score standardized and pooled across water bodies; colors denote water bodies and the dashed line indicates the 1:1 relationship.

Table 3 reports the per-lake validation results as the median across five DEM inversions. For units with relatively stable topology (SAS, SARY, AALS, and CHR), the median ΔH r ranges from 0.90 to 0.99, with a median RMSE of 0.27–2.56 m. SARY achieves the lowest median ΔH RMSE (0.27 m). CHR shows the largest (2.56 m), mainly because regulated intra-annual water-level fluctuations are harder to reproduce. ΔV agreement is similarly strong, with a median r of 0.90–0.99 and a median RMSE of 0.94–2.33 km^3. This indicates that the multi-DEM, multi-model ensemble constraints can effectively control extrapolation errors. For BAS, however, whole-lake modeling still yields high ΔH correlation (r = 0.996) with a median RMSE of ~3 m, but the median ΔV RMSE increases sharply to 62.70 km^3. After sub-lake separation, EBAS and WBAS yield ΔV RMSE of 7.66 and 15.10 km^3, respectively, a substantial reduction from the whole-lake BAS value, while ΔH RMSE remains comparable (3.35 and 2.58 m).

Table 3. Multi-DEM bathymetry model performance and independent validation of monthly water-level and storage changes for major lakes in the Aral Sea Basin (1993–2024).

Lake	N	H–A Fit RMSE (m)	V–A Fit RMSE (km^3)	ΔH r	ΔH RMSE (m)	ΔH MAE (m)	ΔV r	ΔV RMSE (km^3)	ΔV MAE (km^3)
SAS	228	0.03 [0.02–0.11]	0.22 [0.04–0.55]	0.963 [0.963–0.963]	0.57 [0.49–0.61]	0.53 [0.45–0.56]	0.961 [0.961–0.961]	2.02 [1.78–2.13]	1.90 [1.66–1.98]
SARY	232	0.33 [0.10–0.77]	1.56 [0.41–3.75]	0.994 [0.994–0.994]	0.27 [0.24–0.35]	0.22 [0.20–0.31]	0.994 [0.994–0.994]	0.94 [0.89–1.29]	0.78 [0.73–1.08]
AALS	197	0.11 [0.07–0.13]	0.71 [0.41–1.25]	0.901 [0.898–0.902]	0.84 [0.79–1.17]	0.64 [0.61–0.96]	0.900 [0.896–0.900]	2.33 [2.28–5.37]	1.79 [1.74–4.78]
CHR	265	0.06 [0.03–1.19]	1.47 [1.20–2.06]	0.949 [0.948–0.953]	2.56 [1.06–3.50]	1.93 [0.64–2.77]	0.919 [0.918–0.919]	1.93 [1.76–2.14]	1.69 [1.63–1.76]
BAS	87	0.14 [0.12–0.15]	8.26 [6.65–9.21]	0.996 [0.994–0.999]	2.90 [0.22–3.90]	2.34 [0.16–3.14]	0.995 [0.995–0.998]	62.70 [4.41–85.56]	52.43 [3.58–72.28]
EBAS	175	0.15 [0.09–0.21]	6.87 [4.01–7.60]	0.856 [0.838–0.859]	3.35 [2.52–3.50]	2.92 [2.13–3.12]	0.895 [0.892–0.906]	7.66 [2.10–14.23]	7.00 [1.69–13.42]
WBAS	175	0.23 [0.09–0.41]	6.11 [5.23–6.94]	0.997 [0.995–0.997]	2.58 [0.54–4.32]	2.21 [0.45–3.79]	0.995 [0.992–0.996]	15.10 [12.89–17.97]	13.46 [11.36–16.06]

Note: For each lake, results across five DEM inversions (SRTM, NASADEM, ASTER, ALOS, Copernicus) are summarized as median [min, max]. H–A fit RMSE and V–A fit RMSE are model-fitting residuals (H–A and volume, respectively). Validation metrics (r, RMSE, MAE) are computed from month-matched ΔH and ΔV against G-REALM; N is the number of matched G-REALM months.

3.3. Expanding Water Bodies

For expanding lakes, multi-source DEM reconstruction can robustly capture both engineering-driven events and long-term trends. Using SAS and SARY as examples, the reconstructed storage series reproduces key recovery and expansion phases. These changes also agree in magnitude with independent altimetry estimates (Figure 7).

For SAS, the reconstruction reflects a clear storage rebound after the completion of the Kokaral Dam, followed by gradual stabilization (Figure 7a,c,e). The Mann–Kendall test identifies a turning window during 2004–2005, with the G-REALM change point falling in the latter part. During 1993–2004, the area declined at ~31.65 km^2/yr; after a minimum in summer 2005, SAS peaked at 3364.63 km^2 in May 2006 and stabilized. The reconstructed storage increases of 7.04–8.36 km^3 bracket the G-REALM estimate of 6.48 km^3, with Copernicus showing the largest positive bias (+1.88 km^3).

In contrast, Sarygamysh Lake (SARY) shows persistent expansion during 1993–2024 (Figure 7b,d,f). The Mann–Kendall test identifies a significant turning point in April 1999, after which Sen's slope indicates an area increase of ~14.92 km^2/yr (3452.58 km^2 in 1993 to 3915.05 km^2 in 2024). Although DEMs show systematic absolute elevation offsets, ΔH results remain highly consistent (mean cross-DEM difference 0.32 m). The cumulative storage gain of 18.20–19.38 km^3 agrees closely with the G-REALM estimate of 20.29 km^3.

Overall, for expanding water bodies with stable topology, multi-DEM reconstructions identify trends and key events consistently. Estimates of changes also converge well. This provides a reliable baseline for subsequent cross-water-body comparisons.

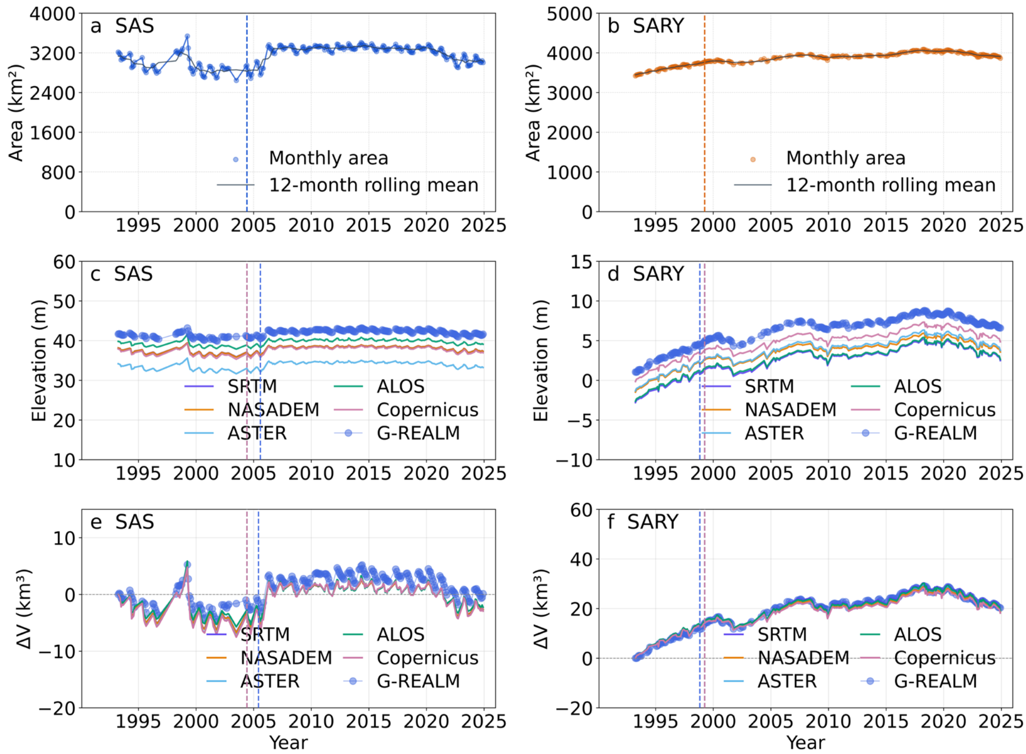

Figure 7. Time series of surface area, reconstructed water level, and volume change for the Small Aral Sea (SAS) and Sarygamysh Lake (SARY) from 1993 to 2024. Panels (**a**,**b**) show monthly lake area (dots) and 12-month rolling mean (line). Panels (**c**,**d**) and (**e**,**f**) display the water level and volume change ΔV reconstructed from five different DEMs (colored lines) compared with G-REALM altimetry (blue dots). The vertical dashed lines indicate the significant regime shift points detected by the Mann–Kendall mutation test.

3.4. Lake Systems and Reservoirs

The Aydar–Arnasay Lake System (AALS) and the Chardarya Reservoir (CHR) represent two typical water bodies that are sensitive to shallow-slope terrain. AALS is a connected lake system, while CHR is controlled by reservoir operations and shows a stable intra-annual rise and fall. Figure 8 compares area, DEM-based reconstructed water level and storage change, and G-REALM estimates. It shows that over low-slope shallow-water terrain, DEM errors translate more readily into storage uncertainty.

For AALS, the area series shows a “fast-then-slow” expansion. During 1993–2005, the system expanded rapidly. Mean annual area increased from 1937.32 km^2 to 3306.91 km^2, a 70.7% rise. The Mann–Kendall test identifies a significant change point in April 1995. During 1993–1995, the expansion rate was 420.30 km^2/yr. After 1995, it drops to 6.67 km^2/yr. The system then remains on a high-area plateau for a prolonged period (Figure 8a). Long-term trends in storage change are broadly consistent across DEMs, but peak magnitude diverges. Comparing cumulative storage changes over 1993–2024, SRTM, NASADEM, ASTER, and Copernicus indicate a cumulative gain of 13.73–14.39 km^3, with a small internal spread. ALOS is systematically lower, with a cumulative gain of 9.8 km^3, about 3.93–4.59 km^3 less than the other four DEMs. The G-REALM mean annual gain is 12.44 km^3, falling between the two groups (Figure 8e). Differences are more pronounced at high-water stages. Over the full record, the peak monthly storage change reaches 24.36 km^3 for NASADEM but only 16.22 km^3 for ALOS, a peak difference of 8.14 km^3. AALS includes extensive shallow flats and spill depressions. Once the lake surface covers these flats, small vertical DEM errors can rapidly translate into large storage differences. As a result, disagreement across DEMs mainly appears in peaks and fluctuation amplitude, rather than in the direction of long-term change.

CHR shows a stable intra-annual cycle in both area and water level (Figure 8b,d). G-REALM provides an intra-annual regulation range of 4.13 ± 0.69 km^3. Copernicus and ALOS bracket this closely at 4.56 ± 1.04 km^3 and 3.61 ± 0.83 km^3, while SRTM, NASADEM, and ASTER show amplified water-level ranges (12.44–14.74 m vs. G-REALM 7.52 ± 1.36 m), reflecting error amplification over the flat reservoir basin. Despite amplitude differences, all reconstructed series remain in phase with G-REALM, confirming that the near-monthly area series stably captures the reservoir's operational rhythm.

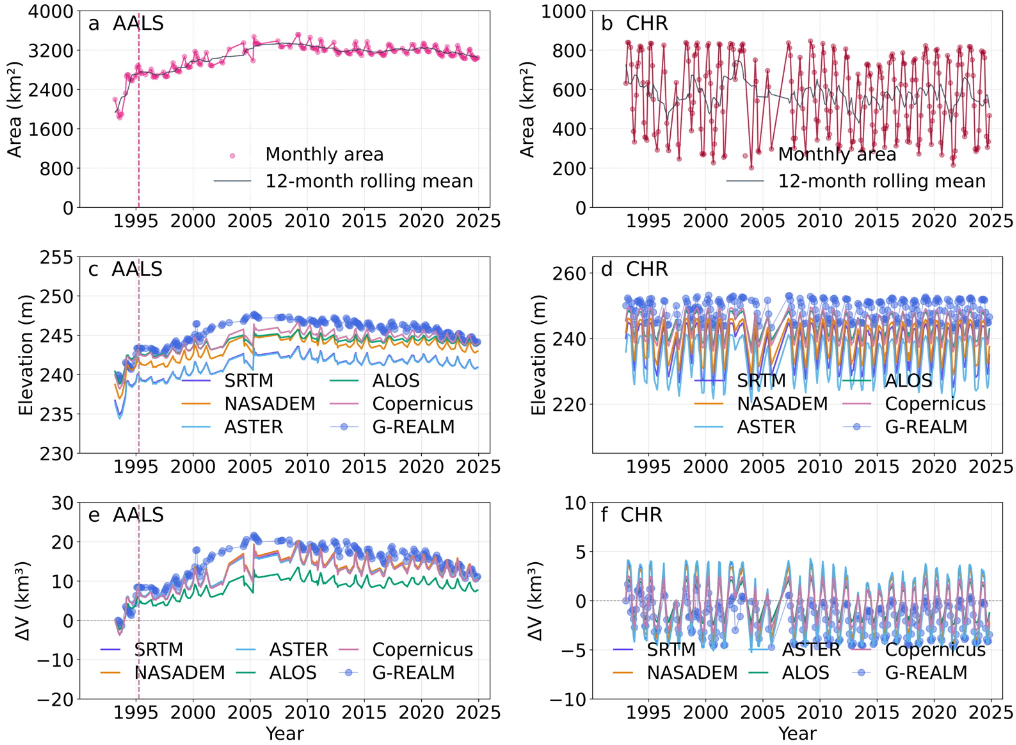

Figure 8. Time series of surface area, reconstructed water level, and volume change for the Aydar–Arnasay (AALS) and Chardarya (CHR) from 1993 to 2024. Panels (**a**,**b**) show monthly lake area (dots) and 12-month rolling mean (line). Panels (**c**,**d**) and (**e**,**f**) display the water level and volume change ΔV reconstructed from five different DEMs (colored lines) compared with G-REALM altimetry (blue dots). The vertical dashed lines indicate the significant regime shift points detected by the Mann–Kendall mutation test.

Overall, differences across DEMs for AALS and CHR mainly appear in peak values and fluctuation amplitude, while long-term trend directions are broadly consistent. For AALS, uncertainty concentrates in peak storage estimates when high water covers shallow flats. For CHR, it concentrates on amplification or compression of the intra-annual regulation range. Over low-slope shallow-water terrain, multi-source DEM ensemble constraints help suppress amplitude bias introduced by noise in any single DEM, and improve robustness for cross-water-body comparison.

3.5. Terminally Shrinking Lakes

Figure 9a documents the evolution of the Big Aral Sea (BAS) from a continuous water body to a fragmented lake-basin system. In 1993, BAS still covered 32,986 km^2, but it declined persistently during 1993–2024, with a Sen's slope of −1016.31 km^2/yr. After disconnection, the East Basin (EBAS) shrank most severely. Its area decreased from 24,780 km^2 to 241.14 km^2 with a Sen's slope of −826.84 km^2/yr, and the main basin largely desiccated and transitioned into a seasonal wetland. The West Basin (WBAS), as the remaining deep-water pool, decreased from 8197.76 km^2 to 1968.80 km^2 at $-$195.93 km^2/yr. The Mann–Kendall test identifies a key morphological transition in 2007–2008. Segment-wise trend analysis shows that EBAS maintained a high shrinkage rate both before and after the change point. In contrast, WBAS shrinkage slowed substantially after the change point; the shrinkage rate magnitude decreased from 285.80 km^2/yr to 144.36 km^2/yr, consistent with a relatively stable deep-water remnant. Figure 9b shows that multi-source DEM reconstructions agree on the overall declining water-level trend, but whole-lake modeling indicates divergent cumulative drawdown. SRTM produces the largest drop, with ΔH of 20.70 m, whereas Copernicus produces the smallest, with ΔH of 12.97 m. Compared with G-REALM, the detected change point for EBAS is broadly consistent: G-REALM indicates July 2008, while the reconstruction indicates April 2007. For WBAS, however, the altimetry-based change point is markedly delayed: G-REALM indicates May 2016, whereas the reconstruction indicates November 2012. This ~4-year offset is attributable to the much shorter G-REALM observation window for WBAS (2005–2024 only; see Figure 2), which truncates the pre-change baseline and shifts the detected turning point later, rather than indicating a systematic reconstruction bias.

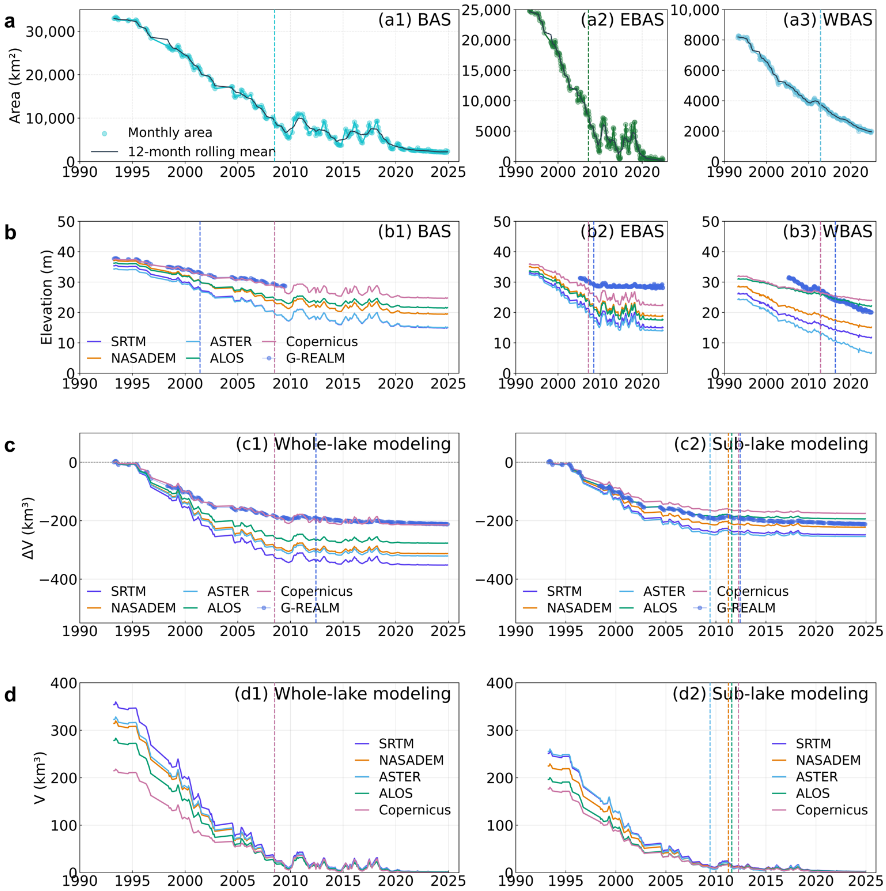

Figure 9. Time series of surface area, reconstructed water level, and volume change for the BAS, EBAS, and WBAS from 1993 to 2024. (**a**) Monthly surface water area derived from Landsat. (**b**) Reconstructed lake surface elevations derived from multi-DEM hypsometry. (**c**) Reconstructed water storage changes relative to the initial state. (**d**) Absolute water storage variations estimated from multi-DEM sources. Vertical dashed lines mark significant regime-shift dates detected by the Mann–Kendall test for the 5-DEM reconstructed series and the G-REALM altimetry series. Note that G-REALM observation windows differ across sub-lakes (BAS: 1993–2008; EBAS and WBAS: 2005–2024; see Figure 2), so the G-REALM-derived change points are not directly comparable with those from the full 1993–2024 reconstruction.

Figure 9c,d further demonstrates the decisive effect of whole-lake modeling versus sub-lake modeling on storage estimates. Under the single-topology assumption, whole-lake modeling relies on early DEMs (SRTM, NASADEM, ASTER, and ALOS), which were acquired at relatively high-water levels and therefore lack below-water detail at low elevations. This leads to systematic overestimation of the initial 1993 storage, with estimates of 353.75, 314.44, 322.64, and 278.32 km^3, as shown in Figure 9(d1). It also inflates the estimated 1993–2024 cumulative storage changes to −351.69, −312.64, −320.79, and −276.83 km^3, as shown in Figure 9(c1). By contrast, the Copernicus-based reconstruction provides a cumulative storage change of −214.30 km^3, closest to the G-REALM estimate of −210.68 km^3, and the time series curves align closely. After introducing sub-lake modeling, estimates from different DEMs converge overall (Figure 9d). For SRTM, the mean annual loss rate decreases from −11.34 km^3/yr under whole-lake modeling to −8.01 km^3/yr, and the cumulative change becomes −248.38 km^3 (Figure 9(c2)), which is much closer to the G-REALM mean estimate of −6.80 km^3/yr. NASADEM and ASTER also converge to −7.17 and −8.20 km^3/yr, respectively. These results indicate that, for early DEMs or DEMs with limited below-water detail, explicitly accounting for fragmented lake topology is essential to reduce structural bias and restore comparability of long-term storage trends.

4. Discussion

4.1. Accuracy and Uncertainty of the Otsu-Derived Area Series as Reconstruction Inputs

We validated the Otsu-derived water areas against manually delineated reference polygons for the Aral Sea sub-lakes over 1993–2020 (Figure 10a–c). Overall agreement is high (R^2 = 0.997, MdAPE = 1.8%, MAE = 276.3 km^2). Positive biases for BAS (+259.8 km^2) and EBAS (+273.6 km^2) are concentrated in 2008–2016, when the eastern Big Aral Sea approached desiccation and the broad, shallow seasonal water bodies [18] produced blurred water–sediment boundaries under near-dry conditions. SAS and WBAS show small negative biases of −26.1 and −14.9 km^2, likely due to sub-pixel mixing at the water–land boundary: when edge pixels have spectra between water and land, a single threshold tends to label them as non-water, causing a slight underestimation of water area [29]. For near-monthly image compositing, we applied a ±10-day temporal buffer to compensate for data scarcity in the early record. Figure 10d shows that the median buffer-filled fraction is very low for most lakes throughout the record; only in the autumn–winter of 1993 does it reach ~48% over the Big Aral Sea region, because Landsat 5 was the only sensor available at that time. As shown in Section 3.2, our area series correlates much more strongly with G-REALM water levels (r = 0.962) than the GSWE Monthly History product (r = 0.480), indicating that our area extraction and quality-control strategy effectively mitigates incomplete lake-surface mapping caused by poor early image quality or high cloud cover and data scarcity in autumn–winter seasons. Figure 10e,f presents the propagated area-uncertainty results. The median σ_H = 0.065 m and σ_V = 0.185 km^3 across all lakes and DEMs, which are small relative to the reconstructed signals (ΔH = 2–20 m, ΔV = 10–350 km^3). Uncertainty depends mainly on shoreline complexity rather than DEM source: from WBAS to AALS, median σ_H increases 17-fold from 0.03 to 0.51 m and σ_V increases 26-fold from 0.06 to 1.54 km^3, while inter-DEM coefficients of variation remain below 10%.

4.2. Multi-Source Cross-Validation of Reconstructed Water Levels

Since each altimetry platform differs in orbit geometry, footprint size, and waveform-processing strategy [6], the G-REALM-only validation in Section 3.2 requires multi-source corroboration. We cross-checked reconstructed water levels against DAHITI [31], Hydroweb, and ICESat/ICESat-2 [32] for six lakes (Figure 11). Topologically stable lakes (SAS, SARY, CHR) yield median r = 0.93–0.99 and RMSE = 0.21–2.50 m across the three platforms; WBAS yields r $\geq$ 0.97. The cross-DEM IQR of r is very narrow (<0.01) for each lake-platform pair, confirming that validation outcomes are insensitive to DEM choice. These results confirm that the G-REALM-based conclusions are not an artifact of the reference chosen. A notable divergence appears for WBAS after ~2020: DAHITI stabilizes near ~23.5 m, while G-REALM and ICESat/ICESat-2 record continued decline to ~20 m. Radar altimetry over shrinking lakes is susceptible to waveform contamination from exposed land [6,33], and different processing strategies handle contaminated returns differently [31,34]. ICESat-2 laser altimetry (~17 m footprint) [32], being less susceptible to land contamination, supports the continued-decline interpretation. After removing trends and monthly climatology, the five natural lakes yield a median r = 0.92 against G-REALM; for CHR, the detrended residual correlation is lower (r = 0.66) because individual regulation events are governed by management decisions rather than by terrain geometry, yet the full (non-detrended) reconstruction remains in phase with G-REALM and reproduces the intra-annual regulation cycle (Section 3.4).

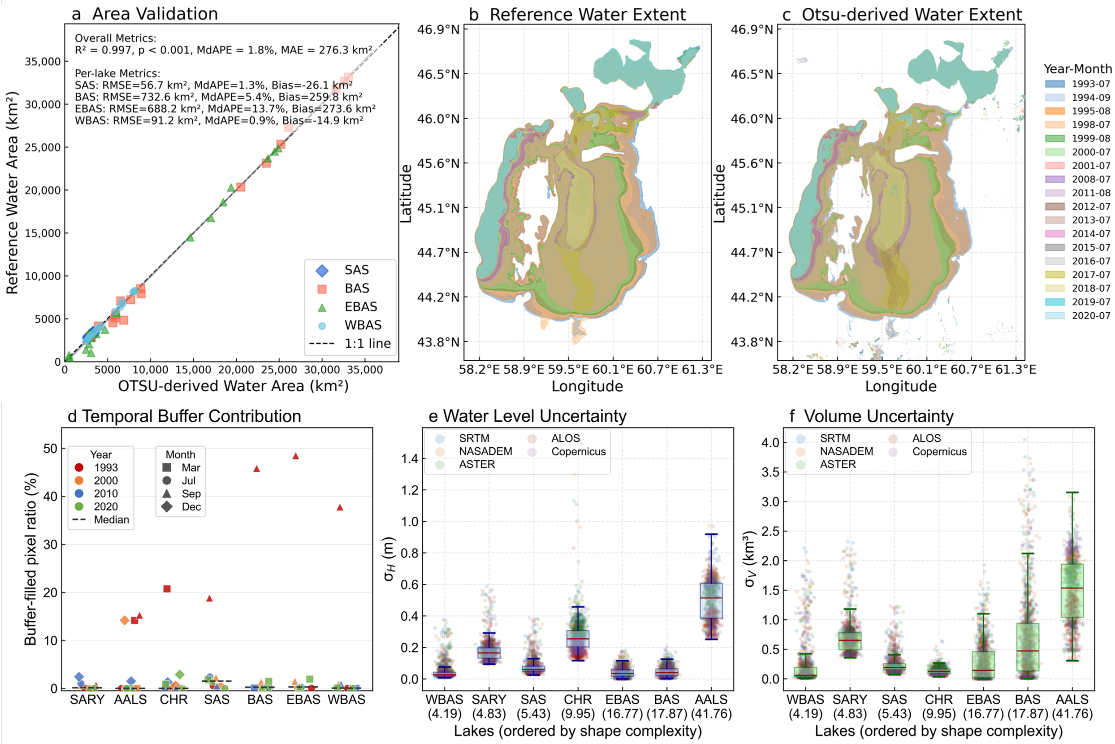

Figure 10. Accuracy and uncertainty assessment of the Otsu-derived monthly water-area series. Panel (**a**) compares Otsu-derived areas with manually delineated reference areas for the four Aral Sea sub-lakes (SAS, BAS, EBAS, and WBAS) over the validation epochs from 1993 to 2020. The dashed line shows the 1:1 reference. Panels (**b**,**c**) map the reference and Otsu-derived water extents for the same epochs, with colors indicating year and month. Panel (**d**) summarizes the contribution of temporal buffering as the share of water pixels supported by buffer-filled observations, and the dashed line marks the median for each lake. Panels (**e**,**f**) show how a $\pm$0.5-pixel shoreline uncertainty propagates into water-level uncertainty σ_H and storage uncertainty σ_V. Lakes are ordered by shoreline complexity, and the boxplots show the median and interquartile range with 1.5 $\times$ IQR whiskers, while points are colored by DEM source.

4.3. Complementary Multi-DEM Hypsometry for Reducing Low-Water Extrapolation Uncertainty Caused by Missing Bathymetry

Submerged topography is often unavailable [8], so DEMs acquired at different water levels serve as the primary geometric constraint. As noted by Liu et al. [12], each DEM's effective range is limited to its acquisition water level; extrapolating beyond that range can produce oscillations or nonphysical departures (Figure 12). For expanding SAS, the 1993–2000 low-water period lies outside early DEM coverage, causing large ΔV oscillations with ASTER. For shrinking EBAS and WBAS, water levels dropped below DEM-constrained ranges, producing nonphysical water-level departures. The Copernicus DEM, acquired during 2010–2015 [35], captures more of the shrinking Aral Sea's basin geometry and therefore performs best for these lakes (Section 3.1; Figure 12a). We therefore treat DEMs from different epochs as complementary sources and build a candidate ensemble across five DEMs and multiple function families. Two-stage screening extracts ensemble-level consensus constraints, so that even if one DEM lacks low-elevation terrain, others compensate—particularly important for lakes with low-gradient shorelines, shallow flats, and saline-crust surroundings [19].

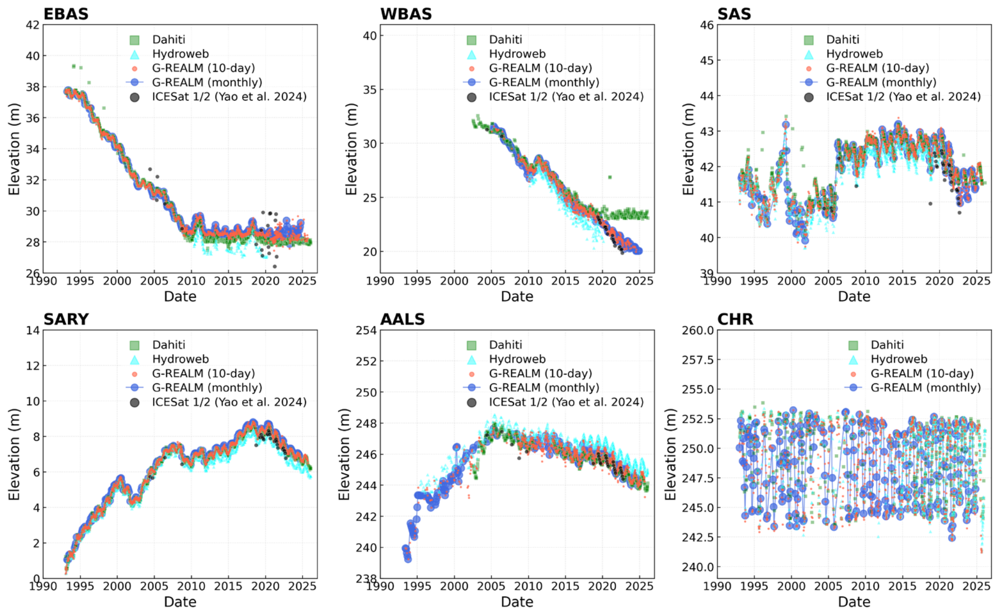

Figure 11. Multi-source altimetry water-level records for the six study lakes. Each panel compares G-REALM monthly and 10-day observations, DAHITI, Hydroweb, and ICESat/ICESat-2 [32].

4.4. Sub-Lake Modeling to Correct Storage Bias Induced by Lake Disconnection

For persistently shrinking lakes, reconstruction errors are not driven solely by missing terrain detail. When a lake fragments into multiple sub-lakes, continued use of a single whole-lake H–A–V relationship introduces structural bias. The Big Aral Sea illustrates this clearly: during 2007–2009, it split into eastern and western water bodies [36,37], requiring separate sub-basin modeling to remain stage-consistent [38]. Continued whole-lake modeling incorrectly counts the exposed ridge–saddle zone as effective water-body geometry, inflating storage at low levels and overstating long-term losses (Figure 9c,d). Table 3 (Section 3.2) confirms that storage error is controlled not only by DEM quality but also by topology change: topologically stable units show strong ΔV agreement with G-REALM, whereas BAS whole-lake modeling produces a sharply higher ΔV RMSE despite comparable ΔH accuracy. We therefore use the remote-sensing area series to detect connectivity changes and, once connectivity breaks, build independent H–A–V relationships for EBAS and WBAS [39,40]. This approach reduces the SRTM-based mean annual loss rate from -11.34 to -8.01 km^3/yr (Figure 9), substantially correcting cumulative bias.

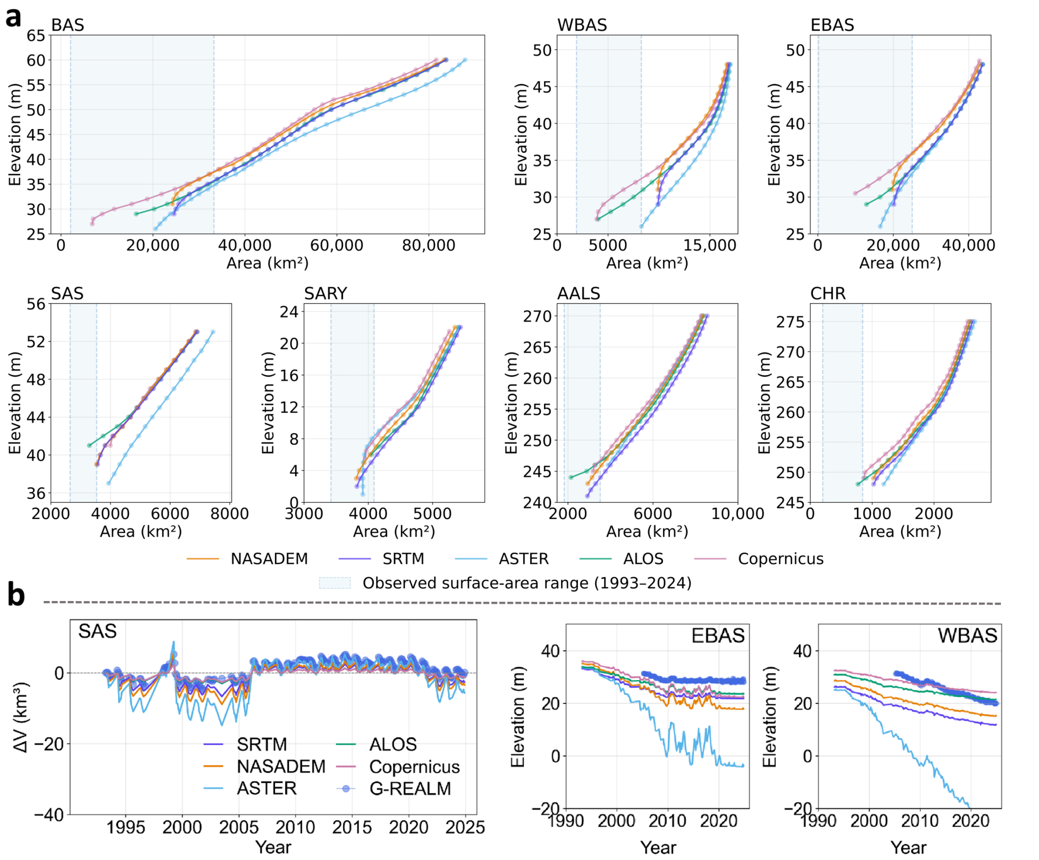

Figure 12. Multi-DEM hypsometric curves and extrapolation failure under simplified model selection. (**a**) Area–elevation relationships of the major study water bodies derived from five DEM products. Hypsometric curves were extracted at 1 m vertical intervals above the water surface from SRTM, NASADEM, ASTER, ALOS, and Copernicus DEMs. The light blue shading marks the observed surface-area range over 1993–2024. (**b**) Representative low-water extrapolation failure cases in storage change (SAS) and water-level reconstruction (EBAS, WBAS) under simplified ranking rules.

4.5. Lake Evolution Under Climate Change and Human Activities

Using the near-monthly area and storage series, we characterize storage variability among major water bodies in the Aral Sea Basin during 1993–2024 (Figure 13; Table 4). The Small Aral Sea stabilized after the Kokaral Dam completion in 2005, as also indicated by the MK change point in June 2004 (Figure 9). The Chardarya Reservoir shows no significant long-term trend under irrigation scheduling [41]. The Aydar–Arnasay Lake System expanded rapidly in the 1990s following episodic spill events [42], with the April 1995 change point marking a sharp deceleration. Sarygamysh Lake exhibits persistent expansion driven by irrigation drainage [43], with cumulative storage gain of 18.20–19.38 km^3, close to the G-REALM estimate of 20.29 km^3.

By contrast, the Big Aral Sea shows severe long-term shrinkage (Section 3.5; Table 4). The WBAS change-point lag between reconstruction and G-REALM (November 2012 vs. May 2016) reflects asymmetric observation windows rather than a reconstruction bias; G-REALM is used here for magnitude validation only.

These patterns reflect compounded climate and human drivers. Under warming, water deficits intensify [44] and evaporation losses accelerate [18]. During 2000–2020, cropland increased by 2291 km^2 and reservoir area by 1183.5 km^2 [45], and 16–34% of runoff was lost through midstream diversion [39]; groundwater contributions remain uncertain (0–30 km^3/yr) [46,47]. The ~20 km^3 storage gain in SARY is consistent with a basin-wide pattern of upstream retention and downstream drainage dominance, aligned with the reported decoupling of arid-region storage from precipitation [48]. The near-monthly storage series better captures these compounded signals than area-only monitoring.

Table 4. Mann–Kendall change points and ΔV Sen's slope for major water bodies in the Aral Sea Basin.

Lake	Reconstructed (5-DEM Median)				G-REALM (Validation Reference)			
	Change Point	Pre-Change (km^3/yr)	Post-Change (km^3/yr)	Full Period (km^3/yr)	Change Point	Pre-Change (km^3/yr)	Post-Change (km^3/yr)	Full Period (km^3/yr)
SAS	2004-06	−0.7	−0.14	0.1	2005-06	−0.36	−0.14	0.17
SARY	1999-04	3.18	0.69	1.16	1998-11	3.17	0.7	1.2
AALS	1995-04	7.45	0.25 [c]	0.45	1994-06	3.59	0.02	0.26
CHR	--	--	--	−0.04	--	--	--	−0.06
BAS (whole-lake)	2008-07	−43.82	−1.6	−7.83	2012-06	−19.12	−1.71	−4.88
BAS (sub-lake) [a]	2009-06 to 2012-04	−24.09	−0.87	−4.21	2012-06 [b]	−19.12	−1.71	−4.88

Note: All change points are significant at α = 0.05 unless marked n.s. [a] DEM-to-DEM spread: ASTER (2009-06) to Copernicus (2012-04). [b] G-REALM windows differ across sub-lakes (BAS: 1993–2008; EBAS/WBAS: 2005–2024; see Figure 2); sub-lake G-REALM change points are for magnitude reference only. [c] Not significant.

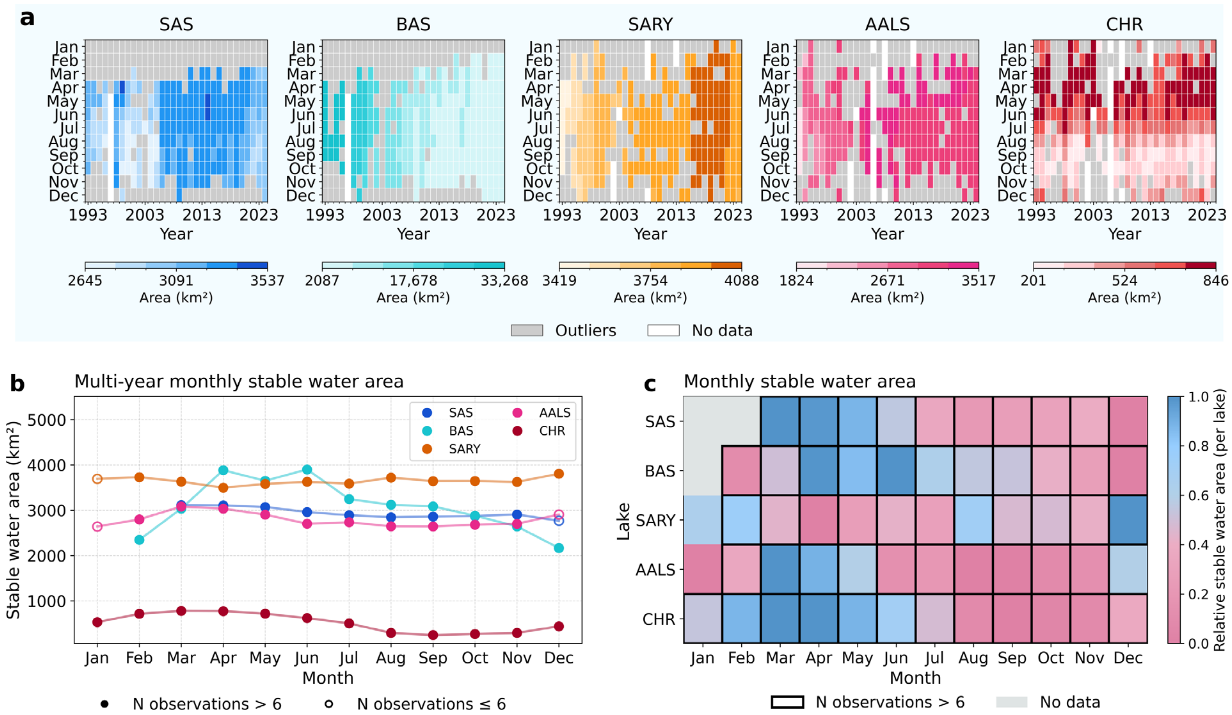

Figure 13. Intra-annual variability and seasonal regimes of large water bodies in the Aral Sea Basin (1993–2024). (**a**) Spatiotemporal matrix heatmaps displaying monthly surface water area dynamics (grey pixels indicate data gaps due to quality control). (**b**) Multi-year mean monthly stable water area (recurrence ≥ 80%). (**c**) Relative seasonal pattern of stable water area, normalized by the lake-specific maximum.

4.6. Framework Robustness and Limitations

We tested the consensus selection method across 33 sensitivity scenarios (Figure 14). Selection consistency exceeds 88.6% for α ≥ 0.5 and reaches 100% at α = 0.8–0.9; pure fit-based ranking (α = 0) reduces consistency to 20% while increasing cross-DEM ΔV RMSE by ~80% (Figure 14a). Under ±50% endpoint weight perturbation, consistency remains ≥ 97.1% (Figure 14c). Three simplified ranking rules perform similarly in overall median ΔV r (0.959–0.961), but produce substantially higher worst-case RMSE for fragmented lakes: EBAS median 7.66 km^3 (this study) vs. 63.07 km^3 (Single-RMSE, 8×); WBAS 15.10 vs. 53.32 km^3 (Figure 14b). The cross-DEM posterior check flags the same 2/35 groups in all

33 scenarios, indicating structural rather than chance anomalies. Because the framework uses only globally available data without in situ calibration, it is directly transferable. Similar DEM-area approaches have been applied at global [12] and regional scales [17]; Yuan et al. [24] demonstrated that DEM choice significantly affects storage estimates, which motivates the consensus-regularized selection adopted here.

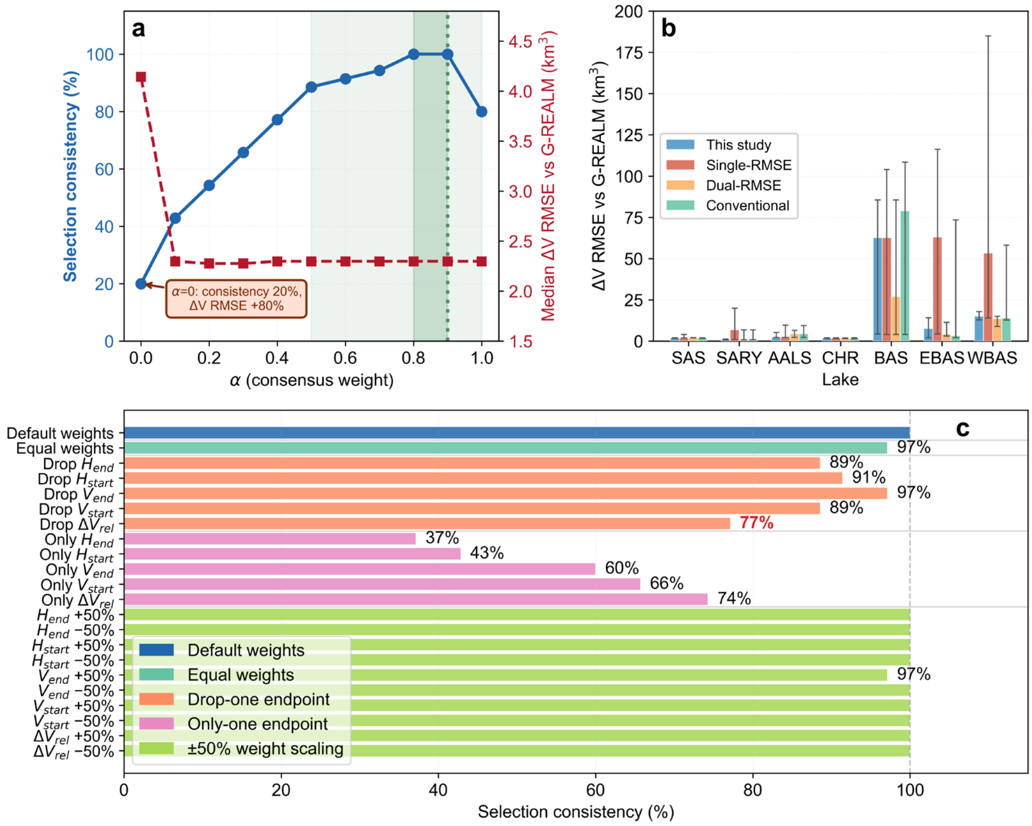

Figure 14. Sensitivity and robustness of the two-stage consensus model selection. (**a**) α-sweep: selection consistency (left axis) and median ΔV RMSE vs. G-REALM (right axis); green band marks α = 0.8–0.9. (**b**) Per-lake ΔV RMSE for four selection strategies. (**c**) Selection consistency under 22 endpoint weight perturbation scenarios.

Two main sources of uncertainty remain. First, DEM vertical errors are spatially heterogeneous and depend on slope and land cover [49]; over shallow flats and salt-crust surroundings, local biases propagate through the area-to-volume mapping. The multi-DEM ensemble treats these as inter-model spread but cannot eliminate correlated errors shared across DEMs. Second, below-water reconstruction assumes bathymetry continues from surrounding topography [9]; long-term sedimentation and erosion can reshape lakebed microtopography. For lakes with limited DEM coverage or a very small area, supplementary constraints, such as satellite altimetry or field surveys, would be needed. Future work should integrate SWOT observations for denser spatial water-level constraints [50] and explore causal inference frameworks to better separate climate variability, reservoir regulation, and water-use shifts as drivers of lake evolution [51].

5. Conclusions

In arid-zone water resource management and water-security assessment, changes in water-body volume are key indicators of water availability and regulation performance. However, insufficient geometric constraints at low water levels, together with hydrological disconnection, can cause unstable extrapolation of water level–storage relationships. This undermines the continuity and comparability of long-term storage time series. To address this, we develop a reconstruction framework that integrates multi-source DEM constraints with the Landsat monthly area series. By complementing low-water geometry, the framework enables continuous long-term storage reconstruction without in situ bathymetric surveys. To improve extrapolation reliability, we propose a two-stage selection strategy. From a multi-DEM, multi-model candidate set, we remove models with unstable extrapolation or overfitting and extract cross-source consistent geometric constraints. This strengthens reconstruction robustness at low water levels. Independent validation against G-REALM altimetry shows strong agreement in both temporal variability and magnitude. Correlation coefficients reach 0.93 for water level and 0.90 for storage change. Performance is markedly better than reconstructions constrained only by above-water topography, $r \approx 0.637$, or selected using conventional model-screening strategies, $r \approx 0.753$.

Across three hydrologic–geometric settings, the framework yields consistent quantitative results. For expanding lakes, reconstructed storage gains for SAS (~7.0–8.4 km^3) and SARY (~18.2–19.4 km^3) agree closely with G-REALM estimates of 6.48 and ~20.3 km^3. For lake systems and reservoirs, AALS storage gains converge across DEMs at 13.7–14.4 km^3, comparable to the G-REALM estimate of ~12.4 km^3. CHR intra-annual regulation ranges from Copernicus and ALOS, which are 4.56 ± 1.04 km^3 and 3.61 ± 0.83 km^3, bracketing the G-REALM value of 4.13 ± 0.69 km^3. Peak storage for AALS remains sensitive to DEM noise over shallow flats, with a peak spread of ~8.1 km^3. For terminally shrinking lakes, sub-lake modeling reduces the SRTM-based cumulative loss from -351.7 km^3 to -248.4 km^3, substantially correcting structural bias from missing below-water terrain detail. The Copernicus whole-lake reconstruction affords -214.3 km^3, closest to the G-REALM estimate of -210.68 km^3. These results confirm H1–H3: multi-DEM consensus screening and topology-aware modeling together deliver robust, transferable storage reconstruction across contrasting arid-zone settings. Overall, this study provides a transferable framework for continuous and comparable storage reconstruction for arid-zone lakes under degraded low-water constraints and hydrological disconnection.

Author Contributions: Conceptualization, S.H., X.C., and X.M. (Xiaoting Ma); methodology, S.H. and X.M. (Xiaoting Ma); software S.H. and L.Y.; validation, S.H., and X.M. (Xuexi Ma); formal analysis, S.H.; investigation, S.H. and H.A.; resources, A.K.K., and I.D.; data curation, S.H., L.L. and B.Y.; writing—original draft preparation, S.H.; writing—review and editing, S.H., X.C., X.M. (Xiaoting Ma) and T.L.; visualization, S.H. and N.W.; project administration, X.C.; funding acquisition, X.C. All authors have read and agreed to the published version of the manuscript.

Funding: This research was funded by Key Program of National Natural Science Foundation of China (42230708), Projects of International Cooperation and Exchanges NSFC (42361144887), Third Xinjiang Scientific Expedition Program (Grant NO. 2021XJKK1300), Joint CAS-MPG Research Project (HZXM20225001MI), Tianshan Talent Project of Xinjiang Uygur Autonomous Region (2022TSYCLJ0056).

Data Availability Statement: The data presented in this study are available in this article.

Acknowledgments: We acknowledge Google Earth Engine for platform support, and thank the providers of Landsat and the global DEM datasets (SRTM, NASADEM, ASTER, ALOS, Copernicus) used in this study. We thank the G-REALM project for providing altimetry validation data.

Conflicts of Interest: The authors declare no competing interests exist in the submission of this manuscript, and the manuscript is approved by all authors for publication. We would like to declare on behalf of our co-authors that the work described was original research that has not been published previously, and is not under consideration for publication elsewhere, in whole or in part.

References

1. Wang, J.; Song, C.; Reager, J.T.; Yao, F.; Famiglietti, J.S.; Sheng, Y.; MacDonald, G.M.; Brun, F.; Schmied, H.M.; Marston, R.A.; et al. Recent global decline in endorheic basin water storages. *Nat. Geosci.* **2018**, *11*, 926–932. [CrossRef]
2. Zhao, G.; Liu, S.; Deng, H.; Tang, Q.; Zhang, C.; Su, Y.; Chen, F. Identifying drivers of storage dynamics of lakes and reservoirs in the arid Central Asia. *Environ. Res. Lett.* **2025**, *20*, 14021. [CrossRef]
3. Li, L.; Long, D.; Wang, Y.; Woolway, R.I. Global dominance of seasonality in shaping lake-surface-extent dynamics. *Nature* **2025**, *642*, 361–368. [CrossRef] [PubMed]
4. Wang, X.; Zhang, J.; Wang, S.; Ge, Y.; Duan, Z.; Sun, L.; Meadows, M.E.; Luo, Y.; Fu, B.; Chen, X.; et al. Reviving the Aral Sea: A Hydro-Eco-Social Perspective. *Earth's Future* **2023**, *11*, e2023E–e3657E. [CrossRef]
5. Huang, S.; Chen, X.; Ma, X.; Fang, H.; Liu, T.; Kurban, A.; Guo, J.; De Maeyer, P.; Van de Voorde, T. Monitoring Surface Water Area Changes in the Aral Sea Basin Using the Google Earth Engine Cloud Platform. *Water* **2023**, *15*, 1729. [CrossRef]
6. Crétaux, J.F.; Abarca-del-Río, R.; Bergé-Nguyen, M.; Arsen, A.; Drolon, V.; Clos, G.; Maisongrande, P. Lake Volume Monitoring from Space. *Surv. Geophys.* **2016**, *37*, 269–305. [CrossRef]
7. Duan, Z.; Bastiaanssen, W.G.M. Estimating water volume variations in lakes and reservoirs from four operational satellite altimetry databases and satellite imagery data. *Remote Sens. Environ.* **2013**, *134*, 403–416. [CrossRef]
8. Khazaei, B.; Read, L.K.; Casali, M.; Sampson, K.M.; Yates, D.N. GLOBathy, the global lakes bathymetry dataset. *Sci. Data* **2022**, *9*, 36. [CrossRef]
9. Messager, M.L.; Lehner, B.; Grill, G.; Nedeva, I.; Schmitt, O. Estimating the volume and age of water stored in global lakes using a geo-statistical approach. *Nat. Commun.* **2016**, *7*, 13603. [CrossRef]
10. Yao, F.; Livneh, B.; Rajagopalan, B.; Wang, J.; Crétaux, J.; Wada, Y.; Berge-Nguyen, M. Satellites reveal widespread decline in global lake water storage. *Science* **2023**, *380*, 743–749. [CrossRef]
11. Huang, W.; Duan, W.; Chen, Y. Unravelling lake water storage change in Central Asia: Rapid decrease in tail-end lakes and increasing risks to water supply. *J. Hydrol.* **2022**, *614*, 128546. [CrossRef]
12. Liu, K.; Song, C.; Zhao, S.; Wang, J.; Chen, T.; Zhan, P.; Fan, C.; Zhu, J. Mapping inundated bathymetry for estimating lake water storage changes from SRTM DEM: A global investigation. *Remote Sens. Environ.* **2024**, *301*, 113960. [CrossRef]
13. Schwatke, C.; Dettmering, D.; Seitz, F. Volume Variations of Small Inland Water Bodies from a Combination of Satellite Altimetry and Optical Imagery. *Remote Sens.* **2020**, *12*, 1606. [CrossRef]
14. Lv, Y.; Jia, L.; Menenti, M.; Zheng, C.; Jiang, M.; Lu, J.; Zeng, Y.; Chen, Q.; Bennour, A. A novel remote sensing method to estimate pixel-wise lake water depth using dynamic water-land boundary and lakebed topography. *Int. J. Digit. Earth* **2024**, *17*, 2440443. [CrossRef]
15. Weekley, D.; Li, X. Tracking lake surface elevations with proportional hypsometric relationships, Landsat imagery, and multiple DEMs. *Water Resour. Res.* **2021**, *57*, e2020WR027666. [CrossRef]
16. Yao, F.; Wang, J.; Yang, K.; Wang, C.; Walter, B.A.; Crétaux, J. Lake storage variation on the endorheic Tibetan Plateau and its attribution to climate change since the new millennium. *Environ. Res. Lett.* **2018**, *13*, 064011. [CrossRef]
17. Li, X.; Long, D.; Huang, Q.; Han, P.; Zhao, F.; Wada, Y. High-temporal-resolution water level and storage change data sets for lakes on the Tibetan Plateau during 2000–2017 using multiple altimetric missions and Landsat-derived lake shoreline positions. *Earth Syst. Sci. Data* **2019**, *11*, 1603–1627. [CrossRef]
18. Huang, S.; Chen, X.; Chang, C.; Liu, T.; Huang, Y.; Zan, C.; Ma, X.; De Maeyer, P.; Van de Voorde, T. Impacts of climate change and evapotranspiration on shrinkage of Aral Sea. *Sci. Total Environ.* **2022**, *845*, 157203. [CrossRef]
19. Farr, T.G.; Rosen, P.A.; Caro, E.; Crippen, R.; Duren, R.; Hensley, S.; Kobrick, M.; Paller, M.; Rodriguez, E.; Roth, L. The shuttle radar topography mission. *Rev. Geophys.* **2007**, *45*, RG2004. [CrossRef]
20. Crippen, R.; Buckley, S.; Agram, P.; Belz, E.; Gurrola, E.; Hensley, S.; Kobrick, M.; Lavalle, M.; Martin, J.; Neumann, M. NASADEM global elevation model: Methods and progress. *Int. Arch. Photogramm. Remote Sens. Spat. Inf. Sci.* **2016**, *41*, 125–128. [CrossRef]
21. Tachikawa, T.; Kaku, M.; Iwasaki, A.; Gesch, D.B.; Oimoen, M.J.; Zhang, Z.; Danielson, J.J.; Krieger, T.; Curtis, B.; Haase, J. *ASTER Global Digital Elevation Model Version 2-Summary of Validation Results*; NASA: Washington, DC, USA, 2011.
22. Takaku, J.; Tadono, T.; Tsutsui, K. Generation of high resolution global DSM from ALOS PRISM. *Int. Arch. Photogramm. Remote Sens. Spat. Inf. Sci.* **2014**, *40*, 243–248. [CrossRef]
23. Franks, S.; Rengarajan, R. Evaluation of Copernicus DEM and comparison to the DEM used for Landsat Collection-2 processing. *Remote Sens.* **2023**, *15*, 2509. [CrossRef]
24. Yuan, C.; Zhang, F.; Liu, C. A Comparison of Multiple DEMs and Satellite Altimetric Data in Lake Volume Monitoring. *Remote Sens.* **2024**, *16*, 974. [CrossRef]
25. Wulder, M.A.; Loveland, T.R.; Roy, D.P.; Crawford, C.J.; Masek, J.G.; Woodcock, C.E.; Allen, R.G.; Anderson, M.C.; Belward, A.S.; Cohen, W.B. Current status of Landsat program, science, and applications. *Remote Sens. Environ.* **2019**, *225*, 127–147. [CrossRef]
26. Birkett, C.M.; Ricko, M.; Beckley, B.D.; Yang, X.; Tetrault, R.L. G-REALM: A lake/reservoir monitoring tool for drought monitoring and water resources management. In *AGU Fall Meeting Abstracts*; American Geophysical Union: Washington, DC, USA, 2017.

27. Fisher, P.F.; Tate, N.J. Causes and consequences of error in digital elevation models. *Prog. Phys. Geog.* **2006**, *30*, 467–489. [CrossRef]
28. Brožová, N.; Baggio, T.; D'Agostino, V.; Bühler, Y.; Bebi, P. Multiscale analysis of surface roughness for the improvement of natural hazard modelling. *Nat. Hazards Earth Syst. Sci. Discuss.* **2021**, *2021*, 3539–3562. [CrossRef]
29. Donchyts, G.; Schellekens, J.; Winsemius, H.; Eisemann, E.; van de Giesen, N. A 30 m Resolution Surface Water Mask Including Estimation of Positional and Thematic Differences Using Landsat 8, SRTM and OpenStreetMap: A Case Study in the Murray-Darling Basin, Australia. *Remote Sens.* **2016**, *8*, 386. [CrossRef]
30. Zhang, G.; Bolch, T.; Chen, W.; Crétaux, J. Comprehensive estimation of lake volume changes on the Tibetan Plateau during 1976–2019 and basin-wide glacier contribution. *Sci. Total Environ.* **2021**, *772*, 145463. [CrossRef]
31. Schwatke, C.; Dettmering, D.; Bosch, W.; Seitz, F. DAHITI—An innovative approach for estimating water level time series over inland waters using multi-mission satellite altimetry. *Hydrol. Earth Syst. Sci.* **2015**, *19*, 4345–4364. [CrossRef]
32. Yao, F.; Livneh, B.; Rajagopalan, B.; Wang, J.; Yang, K.; Crétaux, J.; Wang, C.; Minear, J.T. Leveraging ICESat, ICESat-2, and Landsat for Global-Scale, Multi-Decadal Reconstruction of Lake Water Levels. *Water Resour. Res.* **2024**, *60*, e2023W–e35721W. [CrossRef]
33. Dettmering, D.; Schwatke, C.; Boergens, E.; Seitz, F. Potential of ENVISAT Radar Altimetry for Water Level Monitoring in the Pantanal Wetland. *Remote Sens.* **2016**, *8*, 596. [CrossRef]
34. Shu, S.; Liu, H.; Beck, R.A.; Frappart, F.; Korhonen, J.; Lan, M.; Xu, M.; Yang, B.; Huang, Y. Evaluation of historic and operational satellite radar altimetry missions for constructing consistent long-term lake water level records. *Hydrol. Earth Syst. Sci.* **2021**, *25*, 1643–1670. [CrossRef]
35. Meadows, M.; Jones, S.; Reinke, K. Vertical accuracy assessment of freely available global DEMs (FABDEM, Copernicus DEM, NASADEM, AW3D30 and SRTM) in flood-prone environments. *Int. J. Digit. Earth* **2024**, *17*, 2308734. [CrossRef]
36. Yang, X.; Wang, N.; Chen, A.; He, J.; Hua, T.; Qie, Y. Changes in area and water volume of the Aral Sea in the arid Central Asia over the period of 1960–2018 and their causes. *Catena* **2020**, *191*, 104566. [CrossRef]
37. Micklin, P. The future Aral Sea: Hope and despair. *Environ. Earth Sci.* **2016**, *75*, 844. [CrossRef]
38. Tao, D.; Shi, H.; Gao, C.; Zhan, J.; Ke, X. Water Storage Monitoring in the Aral Sea and its Endorheic Basin from Multisatellite Data and a Hydrological Model. *Remote Sens.* **2020**, *12*, 2408. [CrossRef]
39. Ma, X.; Huang, S.; Huang, Y.; Wang, X.; Luo, Y. Evaporation from the hypersaline Aral Sea in Central Asia. *Sci. Total Environ.* **2024**, *908*, 168412. [CrossRef]
40. Wu, Q.; Yue, H.; Liu, Y.; Hou, E. Geospatial quantitative analysis of the Aral Sea Shoreline changes using RS and GIS techniques. *Earth Sci. Inform.* **2022**, *15*, 137–149. [CrossRef]
41. Crétaux, J.; Biancamaria, S.; Arsen, A.; Bergé-Nguyen, M.; Becker, M. Global surveys of reservoirs and lakes from satellites and regional application to the Syrdarya river basin. *Environ. Res. Lett.* **2015**, *10*, 15002. [CrossRef]
42. Groll, M.; Kulmatov, R.; Mullabaev, N.; Opp, C.; Kulmatova, D. Rise and decline of the fishery industry in the Aydarkul–Arnasay Lake System (Uzbekistan): Effects of reservoir management, irrigation farming and climate change on an unstable ecosystem. *Environ. Earth Sci.* **2016**, *75*, 921. [CrossRef]
43. Touge, Y.; Kobayashi, G.; Khujanazarov, T.; Tanaka, K. Reproduction of historical water balance in the Aral Sea Basin: The physically-based framework to quantify water consumption components in endorheic lake. *J. Hydrol.* **2024**, *640*, 131711. [CrossRef]
44. Yue, B.; Chen, X.; Li, S.; Du, Z.; Wilson, J.; Yang, J.; Jiao, Y.; Huang, S.; Zhou, C. A four-band index for both liquid and solid water and its applications in the Aral Sea Basin. *Sci. China Earth Sci.* **2024**, *67*, 769–788. [CrossRef]
45. Li, Q.; Li, X.; Ran, Y.; Feng, M.; Nian, Y.; Tan, M.; Chen, X. Investigate the relationships between the Aral Sea shrinkage and the expansion of cropland and reservoir in its drainage basins between 2000 and 2020. *Int. J. Digit. Earth* **2021**, *14*, 661–677. [CrossRef]
46. Benduhn, F.; Renard, P. A dynamic model of the Aral Sea water and salt balance. *J. Mar. Syst.* **2004**, *47*, 35–50. [CrossRef]
47. Cretaux, J.; Letolle, R.; Bergé-Nguyen, M. History of Aral Sea level variability and current scientific debates. *Glob. Planet. Change* **2013**, *110*, 99–113. [CrossRef]
48. Zhao, G.; Gao, H.; Li, Y.; Tang, Q.; Woolway, R.I.; Merder, J.; Rosa, L.; Michalak, A.M. Decoupling of surface water storage from precipitation in global drylands due to anthropogenic activity. *Nat. Water* **2025**, *3*, 80–88. [CrossRef]
49. Li, H.; Zhao, J.; Yan, B.; Yue, L.; Wang, L. Global DEMs vary from one to another: An evaluation of newly released Copernicus, NASA and AW3D30 DEM on selected terrains of China using ICESat-2 altimetry data. *Int. J. Digit. Earth* **2022**, *15*, 1149–1168. [CrossRef]
50. Salameh, E.; Desroches, D.; Deloffre, J.; Fjørtoft, R.; Mendoza, E.T.; Turki, I.; Froideval, L.; Levaillant, R.; Déchamps, S.; Picot, N.; et al. Evaluating SWOT's interferometric capabilities for mapping intertidal topography. *Remote Sens. Environ.* **2024**, *314*, 114401. [CrossRef]
51. Runge, J.; Gerhardus, A.; Varando, G.; Eyring, V.; Camps-Valls, G. Causal inference for time series. *Nat. Rev. Earth Environ.* **2023**, *4*, 487–505. [CrossRef]

https://doi.org/10.3390/rs18050763